Materials & Design 257 (2025) 114445

Contents lists available at ScienceDirect

Materials & Design

journal homepage: www.elsevier.com/locate/matdes

Enhancing the high-cycle fatigue strength of Ti-Al-N coated Ti-6Al-4V by residual stress design

A. Gitschthaler [a,*], R. Hahn [a], L. Zauner [a], T. Wojcik [a,b], F. Fahrnberger [c], H. Hutter [c], A. Davydok [d], C. Krywka [d], C. Jerg [e], J. Ramm [e], A. Eriksson [e], S. Kolozsvári [f], P. Polcik [f], H. Riedl [a,b]

[a] Christian Doppler Laboratory for Surface Engineering of High-performance Components, TU Wien 1060 Wien, Austria
[b] Institute of Materials Science and Technology, TU Wien 1060 Wien, Austria
[c] Institute of Chemical Technologies and Analytics, TU Wien 1060 Wien, Austria
[d] Institute of Materials Physics, Helmholtz Zentrum Hereon, 22607 Hamburg, Germany
[e] Oerlikon Balzers, Oerlikon Surface Solutions AG, 9496 Balzers, Liechtenstein
[f] Plansee Composite Materials GmbH, 8698 Lechbruck am See, Germany

ARTICLE INFO

Keywords:
Physical vapor deposition
Thin films
Fatigue
Synchrotron diffraction
Residual stress design

ABSTRACT

Physical vapor deposited coatings are widely utilized as surface protection for metal and ceramic components operating in harsh environments. However, research on the high-cycle fatigue (HCF) life of hard-coated metal substrates has reached contradictory conclusions, leaving it unclear whether ceramic coatings enhance or compromise their fatigue resistance. To improve reliability and extend service life, this study explores the residual stress-dependent influence of arc evaporated TiAlN-based thin films on the fatigue life of Ti-6Al-4V. Therefore, different stress-modifying approaches were implemented, including a substrate bias variation, a Tantalum based alloying strategy, and a specific interlayer design. The combination of high-cycle fatigue tests, synchrotron-based experiments providing depth-resolved stress profiles, and the formulation of a linear-elastic stress-failure model resulted in the following identified relationships: *(i)* A threshold level in the residual compressive stress state must be present in TiAlN-based coatings to prevent deteriorating HCF performance introduced by failure of the ceramic nitride. *(ii)* Once the residual compressive stress field is able to shift fatigue crack nucleation into the bulk titanium alloy, the HCF life increases. *(iii)* The further the residual tensile stress peak is shifted from the bulk material surface — achieved through an optimized residual stress design implementing a metallic interlayer beneath the TiAlN-based top coating — the greater the improvement in HCF strength. Overall, this approach achieved an unprecedented HCF enhancement exceeding 50 % compared to uncoated Ti-6Al-4V (from 420 MPa to 628 MPa at 10^7 load cycles), highlighting the importance of an in-depth understanding of stress gradients within coating-substrate combinations.

1. Introduction

Ti-6Al-4V is widely used in aerospace industry due to its high specific strength, excellent corrosion resistance and validated long-term fatigue data [1]. Yet, its insufficient wear resistance can be problematic in components subject to tribological contacts above 500 °C [2–5]. To address these concerns, physical vapor-deposited ceramic coating materials have proven to be an effective surface-strengthening technique [6–9] – in particular nitrides, such as TiAlN-based coatings well-known from tooling and forming applications. At first glance, the deposition of a brittle ceramic coating appears generally unfavorable for the fatigue properties of a ductile metallic component. Due to the strong directionality of their atomic bonds, the dislocation mobility of ceramic materials is typically severely restricted [10]. In contrast to metals, ceramics are unable to relieve the localized stress peaks at the crack front by plastic deformation. Consequently, ceramic bulk and coating materials are characterized by a low fracture toughness and a tendency to exhibit unstable crack growth past the initial fracture event [11,12]. Accordingly, Zauner et al. [13] demonstrated that the micro-scale fatigue response of isolated ceramic coatings (variety of CrN, CrB_2, or

* Corresponding author.
E-mail address: arno.gitschthaler@tuwien.ac.at (A. Gitschthaler).

https://doi.org/10.1016/j.matdes.2025.114445
Received 10 March 2025; Received in revised form 22 May 2025; Accepted 21 July 2025
Available online 23 July 2025

Cr_2O_3) is constrained by the intrinsic fracture strength. In their in-depth study, microcantilever beams were exposed to cyclic loads close to the critical stress intensity and withstood up to 10^7 load cycles without inducing any noticeable material damage or structural changes. Nevertheless, these findings do not explain how ceramic coatings affect the fatigue properties of underlying metallic substrate materials. Understanding the importance of each influencing parameter is critical to eliminating diminishing correlations and making its application safer and more predictable.

Consequently, the impact of ceramic nitrides such as TiAlN-based coatings on the fatigue life of titanium alloys has been the subject of several studies so far. Up to date, it is known that the stress state [14–17], thickness [15,18], quality [16,18,19], and mechanical properties [18,20,21] of the ceramic coating play an important role. Unfortunately, most of the assumptions are based on limited fatigue data, and no general optimization approach has yet been developed. Nevertheless, current studies agree that the conventional "notch effect" model — which claims that coating failure promotes and accelerates fatigue crack initiation due to increased stress concentration on the substrate near interface [22–24] — is unable to describe the experimentally observed changes in fatigue fracture morphology and crack nucleation location for coated Ti-6Al-4V [17,21]. Thus, Bai et al. [17] put forth a "film induced cracking of substrate" model that exhibits a sharp transition between the following two failure modes.

Under elevated stress (typically low-cycle fatigue (LCF) regime), the ceramic coating cannot withstand the large deformation of the metallic substrate. As a result, premature coating fracture results in substrate cleavage cracking. Consequently, the detrimental effect of thin film rupture can only be alleviated by reducing the kinetic energy of the crack reaching the coating interface. For a fixed coating thickness, microstructure toughening, increased compressive stresses, or the introduction of a ductile interlayer may reduce the crack velocity below its critical value. Thereby, the underlying titanium alloy is prevented from fracturing and its low-cycle fatigue limit is improved. In contrast, at reduced applied stresses (typically high-cycle fatigue (HCF) regime), coating failure is caused by substrate dislocation pile-up and slip step formation at the coating-substrate interface. As the crack extends towards the surface, the interface near substrate region is subjected to increasing stress concentrations, which eventually results in subsurface shear fracture. Hence, once the ceramic coating is capable of suppressing the formation of persistent substrate slip steps without cracking, the high-cycle fatigue properties of the material combination are enhanced.

In early 2023, Wang et al. [21] confirmed and extended Bai's proposed fatigue crack initiation model, by examining the fracture morphology and quantifying the geometric dislocation density of ceramic coated Ti-6Al-4V substrates. In contrast to the uncoated titanium alloy, where dislocations slip out of the free surface during cyclic loading, dislocation accumulation is observed at the coating-substrate interface. If the brittle coating cannot resist cracking, notch effects lead to increased stress concentrations on the substrate and promote the initiation of subsurface fatigue crack initiation. However, as soon as film rupture can be prevented, the local stress concentrations at the interface are relieved by the distribution of dislocations and the buildup of secondary slip systems. As a result, crack nucleation shifts deeply into the interior of the titanium alloy, where it is likely caused by differing elastic modulus of adjacent grains. Consequently, in order to optimize the high-cycle fatigue strength of a ceramic coating on top of a metallic substrate, it is of critical importance to suppress coating fracture even at elevated subsurface strains and to push crack initiation far into the bulk material.

Although the proposed stress-sensitive fatigue crack initiation mechanisms appear to be well founded, the model has yet to be experimentally correlated with PVD deposition parameters in order to ultimately establish a quantitative relationship between load cycles and load amplitudes. Therefore, the presented study comprehensively screens three different approaches adapting the stress evolution and relation between coating and substrate material: *(i)* varying stress states by deposition parameter modification, *(ii)* alloying concept adapting the coating material itself, *(iii)* and a specific interlayer design. An in-depth understanding is provided by a set of high-resolution techniques such as HR-TEM, t-EBSD, ToF-SIMS, transmission X-ray nano diffraction, and combined micro-mechanical synchrotron-based experiments. Finally, the findings are incorporated into a linear-elastic stress-failure model, which provides analytical proof of the identified relationships and guidelines to further enhance the fatigue life of hard-coated metallic components.

2. Experimental procedures

2.1. Coating deposition

TiAlN-based thin films were deposited on customized Ti-6Al-4V fatigue specimens (ASTM B265-20 Grade 5; $R_m = 1009$ MPa; $R_{p0.2} = 983$ MPa; $H = 335.8$ HV5) using cathodic arc evaporation in an industrial PVD system (Oerlikon Balzers, INNOVA 1.0). For each deposition process, six-inch powder-metallurgically manufactured targets from Plansee Composite Materials GmbH were operated in a pure N_2-atmosphere: Either four TiAl targets with equal atomic percentages or four TiAlTa targets with a composition of 45/45/10 at. %, respectively. For samples prepared with a metallic interlayer a pure Ar-atmosphere and two Ti targets (purity 99.6 %, Plansee Composite Materials GmbH) were operated. For all deposition runs a variety of materials were mounted on the two-fold rotating columns of the substrate carousel: low-alloy steel (90MnCrV8, $\varnothing 22 \times 5.6$ mm^3), polished Ti-6Al-4V ($10 \times 10 \times 1$ mm^3), polished austenite ($20 \times 7 \times 0.8$ mm^3) and ($10\bar{1}1$)-oriented sapphire ($10 \times 10 \times 0.53$ mm^3). For all fatigue tests, pre-notched custom-made Ti-6Al-4V fatigue samples have been used – see Fig. A1**a** in the Appendix. Prior to each deposition run, the arithmetic mean of the surface height (S_a) of the area between both notches (2.25 mm^2) and the exact notch geometry of the fatigue samples were determined using a Keyence VHX6000 digital microscope (see also Fig. A1**c in the** Appendix). Subsequently, all substrates were pre-cleaned in an ultrasonic bath using acetone and ethanol for five minutes each. The cleaned fatigue specimens were clamped on the sample end opposite to the notch and placed on a rotating support structure inside of the vacuum chamber. This ensured a continuous three-fold rotation during deposition, promoting the formation of a uniform coating on all sides of the fatigue specimen and in particular the notch area. As soon as an adequate vacuum was reached, the chamber was heated to 450 °C, followed by an argon etching step at a gas pressure of 0.22 Pa. Then, a 300 nm thin titanium interlayer was coated on selected samples at a bias voltage of −150 V. Therefore, the targets were subjected to an arc current of 160 A. Subsequently, each titanium aluminum nitride based top-coating was deposited at a total N_2 pressure of 3.2 Pa and an arc current of 200 A. For the residual stress variation, the bias voltage (U_S) was either set to −20, −40 or −80 V, respectively. Moreover, the deposition time was adjusted individually to achieve a total film thickness of about 4500 nm for all coating states.

2.2. Coating characterization

To quantify the top-coating thickness and thus the deposition time, a calotte grinding test was conducted with the BAQ kaloMAX II and the resulting wear marks were evaluated with the Keyence VHX6000 digital microscope. However, a more precise method was necessary for the determination of the interlayer thickness. Therefore, coated Ti-6Al-4V substrates were cut in half with a Struers Accutom-10, heat embedded using Struers CitoPress-30 and polished with a Struers TegraPol-31 system. Finally, scanning electron microscopy (SEM) was employed to analyze the cross sections with a backscattered electron detector (BSD) on a ZEISS Sigma 500 VP. For each coating, the determination of the chemical composition, energy dispersive X-ray spectroscopy (EDS) was

carried out in top-view configuration with an EDAX EDS detector (15 kV acceleration voltage). Furthermore, the structural constitution was analyzed by X-ray diffraction (XRD) using a PANalytical XPert Pro MPD system with a Cu-K α radiation source ($\lambda = 1.5418$ Å) in the Bragg-Brentano geometry. High resolution transmission electron microscopy (HR-TEM) on a FEI TECNAI F20 system (200 kV acceleration voltage) provided information on the growth characteristics and grain size distribution. In addition, transmission electron backscatter diffraction (t-EBSD) was utilized to gain deeper insights into the characteristics of the interface, grain size, and crystal orientation. Accordingly, transmission Kikuchi diffraction patterns were acquired using EDAX Apex 3.0 software and subsequently post-processed with EDAX OIM 8.6.

Indentation hardness (H) and Young's modulus (E) of the TiAlN-based thin films were determined using a CSIRO UMIS nano-indentation system equipped with a Berkovich diamond tip. Prior to the measurements, the system was calibrated with a fused silica standard ($E = 72.5$ GPa, $H = 10$ GPa). To improve the surface quality of the arc evaporated coatings for the indentation tests, all samples were polished with diamond paste to remove macroparticles and achieve a smooth surface. Subsequently, 31 indents ranging from 3 to 45 mN were performed and analyzed according to Oliver and Pharr [25] and Fischer-Cripps [26]. To minimize substrate interference, only indentations with a depth of less than 10 % of the coating thickness were considered. In addition, micromechanical bending experiments were conducted to obtain the fracture toughness (K_{IC}) of selected coating states. Therefore, pre-notched (bridge notch type) micro-cantilevers were prepared by focused ion beam (FIB) milling using Ga^+-ions with an acceleration voltage of 30 keV and an ion current down to 50 pA on a ThermoFisher Scios II – in accordance with the guidelines set forth by Brinckmann et al. [27]. The free-standing thin film material was then placed in a Zeiss Sigma 500 VP and in-situ loaded by the diamond wedge tip using a FemtoTools FT-NMT04 nanoindentation system under displacement-control (10 nms^{-1}) until fracture. Afterward, we evaluated the continuously recorded force–displacement data of the purely linear-elastic material behavior according to Matoy et al. [28]:

$$K_{IC} = \frac{F_{max} L}{B H^{\frac{3}{2}}} f\left(\frac{a}{H}\right) \tag{1}$$

$$f\left(\frac{a}{H}\right) = 1.46 + 24.36\left(\frac{a}{H}\right) - 47.21\left(\frac{a}{H}\right)^2 + 75.18\left(\frac{a}{H}\right)^3 \tag{2}$$

where F_{max} is the maximum load applied, L is the length between the pre-notch and the indenter tip, B is the width of the cantilever, H is the height of the cantilever, and a is the depth of the FIB-made notch.

For the evolution of the residual in-plane stress state of the TiAlN-based top-coatings, the $\sin^2(\psi)$-method was employed [29]. Accordingly, a PANalytical Empyrean system equipped with a Cu-K α radiation source ($\lambda = 1.5418$ Å) was operated in Bragg-Brentano configuration. From the recorded XRD data, the interplanar spacing ($d_{hkl}(\psi)$) was determined by peak fitting using the Highscore Plus software package [30]. To account for the actual anisotropic behavior of elasticity in crystalline thin films, diffraction elastic constants, s_1^{hkl} and $\frac{1}{2}s_2^{hkl}$, of the (200)-diffraction peak were calculated using the single crystal elastic constants of cubic $Ti_{0.5}Al_{0.5}N$ [31] and the inverse Kröner model via the software package IsoDEC [32].

A TOF-SIMS 5 instrument from ION-TOF GmbH, Münster, Germany, was utilized to study potential correlations between the deposition process and nitrogen diffusion of a plasma annealed, a TiAlTaN, and a Ti & TiAlTaN coated fatigue specimen. The plasma annealed sample, which was placed fully covered in the chamber of the PVD system so that it was only exposed to the temperature program of the deposition process, served as a reference for the coated samples. To address the known insensitivity of time-of-flight secondary ion mass spectrometry (ToF-SIMS) for detecting pure nitrogen [33] — despite its high sensitivity and versatility for chemical characterization of inorganic and organic surfaces and interfaces [34] — was addressed by measuring the CN^- signal in a provided methane atmosphere. This offers the advantage of tracking the nitrogen sensitively as the carbon was then the non-limited component. A focused 25 keV Bi^+ ion beam was used as a primary ion source to generate secondary ions within a common field of view (FOV) of 100×100 μm^2. All measurements were conducted with a pulse length of 13 ns and 128×128 pixels in sawtooth rendering. The chosen measurement mode, in negative polarity, was the high current bunched (HCBU) mode, which offers high mass resolution (11000) and DC-currents of 15 nA [35]. To obtain depth information, the dual source column (DSC) was operated with 2 keV Cs^+ ions (300×300 μm^2, 160 nA) for sputtering, and an extraction bias of −20 V was applied to the extractor. For charge compensation, the electron flood gun (21 V) was activated to measure depth profiles in non-interlaced cycle mode (10 s sputtering; 0.5 s pause). The depths of the analysis craters were measured using a Dektak XT profilometer from Bruker to convert the sputter time scale to a depth scale.

2.3. Fatigue testing

Within this study, a so far unprecedented approach was followed for high-cycle fatigue testing using a dynamic mechanical analyzer (DMA) in a single cantilever geometry. To our knowledge, this non-standard method has only been employed for low-cycle fatigue testing of thin samples of zirconium alloys [36,37] as well as nanocomposite [38,39] and shape memory alloy [40] wires. All fatigue experiments were conducted with Ti-6Al-4V fatigue specimens in single cantilever configuration at room temperature, an applied stress ratio (R) of −1, and a frequency (f) of 10 Hz. High-cycle fatigue tests that reached 10^6 load cycles without failure were stopped and considered as the fatigue limit of the coating-substrate combination. The general dimensions of the custom-made Ti-6Al-4V fatigue specimens are illustrated in Fig. A1**a**, and their fully equiaxed microstructure is shown in Fig. A1**b** in the Appendix.

Prior to each measurement, the sample was mounted evenly with a torque wrench, to avoid twisting or distortion. Subsequently, the non-contact and low-mass direct drive motor of the utilized TA Instruments Discovery DMA 850 precisely applied a constant sinusoidal deformation force (P) in the range of 7.5 to 17.5 N. This vertical cyclic movement of the actuated clamp resulted in an inhomogeneous stress distribution. The stress value peaked in the outermost fiber of the specimen and decreased linearly along the cross section until it reached zero at the axis of symmetry of the specimen. Due to the single cantilever configuration, the boundary conditions are

$$w(x = 0) = 0, w'(x = 0) = 0, w'(x = l) = 0 \tag{3}$$

with w being the displacement in z-direction (see Fig. A2**a**). Thus, the bending moment distribution results in

$$M_B(x) = P\left(\frac{l}{2} - x\right) \tag{4}$$

with the maximum bending moment ($M_{B,max} = P\frac{l}{2}$) located directly at the clamps. Linear theory of elasticity yields

$$\sigma_{B,max} = \frac{M_{B,max}}{W} = \frac{3Pl}{bt^2} \tag{5}$$

where l is the distance between the two clamps, t is the sample thickness, and b is the sample width. However, with respect to the geometry of the fatigue specimens designed and used in this work, $\sigma_{B,max}$ represents only the nominal stress. The sharp stress peak in the notch root must be accounted for by the introduction of a notch coefficient (k_B)

$$k_B = \frac{2(1+\nu)\sqrt{\frac{a}{\rho}}}{(3+\nu)arctan\sqrt{\frac{a}{\rho}} - \frac{(1-\nu)\sqrt{\frac{a}{\rho}}}{\frac{a}{\rho}+1}} \tag{6}$$

where the reduced half sample width at the notch is denoted by a, while ρ represents the radius of curvature [41]. Since all specimen are mounted so that the notch is precisely aligned with the fixed clamp (see Fig. A2**b, c**), the maximum applied stress at the notch is given by

$$\sigma_{K,a,max} = \sigma_{B,max} k_B = S \tag{7}$$

To establish a qualitative relationship between load cycles (N) and load amplitude (S), the Basquin relationship

$$log(N) = C_a - C_b log(S) \tag{8}$$

was used on a double logarithmic scale. By approximating the test results, the constant values of the fatigue coefficient (C_a) and the fatigue exponent (C_b) were determined.

2.4. Synchrotron X-ray nanodiffraction experiments

All X-ray nanodiffraction experiments were carried out at the nanofocus endstation of beamline P03 of PETRA III at "Deutsches Elektronen-Synchrotron" DESY (Hamburg, Germany). This high-brilliance synchrotron facility can focus monochromatic X-ray beams to a rectangular probe cross-section of $250x250\ nm^2$. The positioning of the entire nanoindenter (FemtoTools FT-NMT04) and sample arrangement was conducted using a hexapod (tilt alignment) and linear nanopositioning stages (X-, Y-, and Z-alignment). The Debye-Scherrer rings were captured by an Eiger X M9 photon-counting detector, with each frame acquired over a duration of 10 s. The precise alignment of the detector relative to the sample position was calibrated using a standardized LaB_6 reference powder.

To investigate the residual stress gradients of TiAlN-based coated Ti-6Al-4V specimens, transmission X-ray nanodiffraction experiments were carried out [42]. Therefore, the polished cross-section of a coated substrate was first precisely aligned with the monochromatic high-energy X-ray beam ($\lambda = 0.6294$ Å, 19.7 keV), so that its focal point was located in the center of the coating and the substrate-coating interface was parallel to the beam direction. Subsequently, the sample was scanned vertically three times with a step size of 100 nm, starting in the air above the coating and ending a few micrometers deep in the substrate. The sample was shifted 5 µm in the Y-direction after each measurement to capture a different cross-section segment during each line scan. For further details regarding the sample-beam alignment and the referenced coordinate system see Fig. 1**a**.

Coupled microcantilever bending and transmission X-ray nanodiffraction experiments were conducted to analyze the resulting stress behavior of coated Ti-6Al-4V. Accordingly, the previously mentioned FIB workstation was employed to ion-mill thick microcantilevers ($l \times b \times h = 92 \times 29 \times 24\ \mu m^3$) exhibiting a notch geometry comparable to that of the fatigue specimen. Before each measurement, the monochromatic X-ray beam ($\lambda = 0.8266$ Å, 15.0 keV) was positioned at the pre-notch. At the same time, the diamond wedge tip of the nanoindentation system was located at the free end and centered along the width of the 4 µm coated Ti-6Al-4V cantilever sample (see Fig. 1**b**). Area scans were performed to characterize the cross-sectional area around the pre-notch position of unloaded and in-situ loaded specimens. These scans covered a 40×16 mesh grid in steps of 250 nm along the Z-direction and 500 nm along the Y-direction.

Subsequently, the recorded diffraction patterns were processed using the open-source software package DPDAK [43] and an in-house written MATLAB script [44] or the X-ray diffraction data analysis suite Pydidas [45]. By integrating the diffraction rings in segments of 10° from $\delta = -5$ to 95°, the interplanar spacing ($d_{hkl}(\delta)$) for a specific orientation δ was retrieved. Under the assumption of isotropic material behavior and biaxial stress state, the orientation-dependent lattice strain ($\varepsilon_{hkl}(\delta)$) is expressed as [29]

$$\varepsilon_{hkl}(\delta) = \frac{d_{hkl}(\delta) - d_{0,hkl}(\delta^*)}{d_{0,hkl}(\delta^*)} \tag{9}$$

Accordingly, for a given orientation δ, it solely depends on the interplanar spacing of the unstressed material ($d_{0,hkl}(\delta^*)$), which itself can be obtained by performing a linear regression of the $d_{hkl}(\delta) - sin^2(\delta)$. By considering small Bragg angles (θ) and the fundamental equation of X-ray stress analysis [29]

$$\varepsilon_{hkl}(\psi) = \frac{1}{2} s_2^{hkl} \sigma_{r,\parallel} sin^2(\delta) - 2 s_1^{hkl} \sigma_{r,\parallel} \tag{10}$$

the residual in-plane stress ($\sigma_{r,\parallel}$) can be evaluated from the distortion of Debye-Scherrer rings expressed by the term [46]

$$\frac{\partial d_{hkl}(\delta)}{\partial sin^2(\delta)} = \sigma_{r,\parallel} \frac{1}{2} s_2^{hkl} d_{0,hkl}(\delta^*) \tag{11}$$

The diffraction elastic constants, s_1^{hkl} and $\frac{1}{2}s_2^{hkl}$, of various diffraction peaks were calculated utilizing the single crystal elastic constants of cubic $Ti_{0.5}Al_{0.5}N$ [31] ($s_1^{200} = -0.585 \times 10^{-3}$ GPa^{-1}; $\frac{1}{2}s_2^{200} = 3.075 \times 10^{-3}$ GPa^{-1}; $s_1^{111} = -0.482 \times 10^{-3}$ GPa^{-1}; $\frac{1}{2}s_2^{111} = 2.764 \times 10^{-3}$ GPa^{-1}) or hexagonal α-titanium [47] ($s_1^{101} = -2.797 \times 10^{-3}$ GPa^{-1}; $\frac{1}{2}s_2^{101} =$

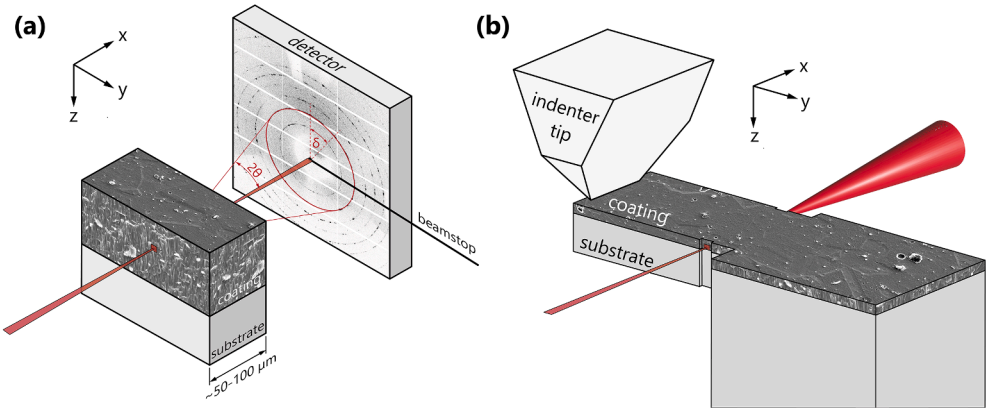

Fig. 1. (a) Schematic representation of the synchrotron transmission nanodiffraction experiments. The crystallinity of the material leads to diffraction of the incident X-ray beam, and the Debye-Scherrer rings are recorded by a 2D detector [48]. (b) For in-situ bending of the microcantilever (l x b x h = 92 x 29 x 24 µm^3), the diamond wedge tip of the nanoindentation system was placed at its free end.

11.407×10^{-3} GPa^{-1}; $s_1^{102} = -2.682 \times 10^{-3}$ GPa^{-1}; $\frac{1}{2}s_2^{102} = 11.072 \times 10^{-3}$ GPa^{-1}) and the inverse Kröner model through the software package IsoDEC [32].

3. Results

In order to assess the significance of the numerous fatigue variables identified in literature, three different approaches focusing on the residual stress state (and related measures) were conducted: *(i)* modifying the bias voltage for stress variation, *(ii)* widening the ternary $Ti_{1-x}Al_xN$ to a quaternary $Ti_{1-x-y}Al_xTa_yN$ system to influence the mechanical properties and stress states, and *(iii)* introducing a metallic titanium interlayer for an interface-based stress design. With regard to *(ii)*, tantalum was selected as the doping element, given that the enhanced properties of the resulting metastable solid solution are well documented in the literature [7,49–54]. For simplicity, each investigated coating system is hereafter defined by the following nomenclature: Those systems without an interlayer are characterized by their chemical composition and their residual stress state, for example $Ti_{0.56}Al_{0.44}N^{-1.29}$. In addition, interlayer systems are marked by Ti & $Ti_{0.48}Al_{0.38}Ta_{0.14}N^{-1.64}$. In order to facilitate the reference to the chemical composition, the ratio of nitrogen to metal has been normalized to 1. All details can be found in Table 1. Prior to the detailed presentation and discussion of the experimental fatigue results, it is important to clarify some general properties of the coating states for the subsequent discussion.

3.1. Structural, chemical, and mechanical constitution

Each coating state was deposited with a thickness of approximately 4500 nm on fully equiaxed Ti-6Al-4V fatigue specimens using cathodic arc evaporation. Due to the strongly fluctuating and uneven surface conditions of the uncoated fatigue samples (S_a ranging from 0.5 to 1.5 μm within the region between both notches), it can be concluded that the surface texture of the coated substrates is not significantly affected by the presence of macroparticles (see Fig. A1**c**). It should be noted that the surface of the fatigue specimens was deliberately left unpolished after manufacture in order to more accurately reflect the real conditions in which the parts would be coated, thereby ensuring that the results are as relevant as possible to practical manufacturing scenarios. Examining the chemical composition, each $Ti_{1-x}Al_xN$ coating exhibits an aluminum content (x) of x 44 at.%, indicating the well-known Ti substitution by Al in the face centered cubic structure [55–57]. Furthermore, the $Ti_{1-x-y}Al_xTa_yN$ coatings contain a tantalum content (y) of 14 at.%, thus falling in the proposed range of further enhanced thermo-mechanical properties [7,49–51]. Moreover, XRD measurements confirmed, that all TiAlN-based coatings are exclusively present in the face-centered cubic crystal structure, and no unwanted hexagonal wurtzite phase formed (see Fig. 2). Since the thermo-mechanical properties of TiAlN coatings are closely related to their phase evolution, already the transition to a dual phase structure is detrimental [8,58]. In accordance with

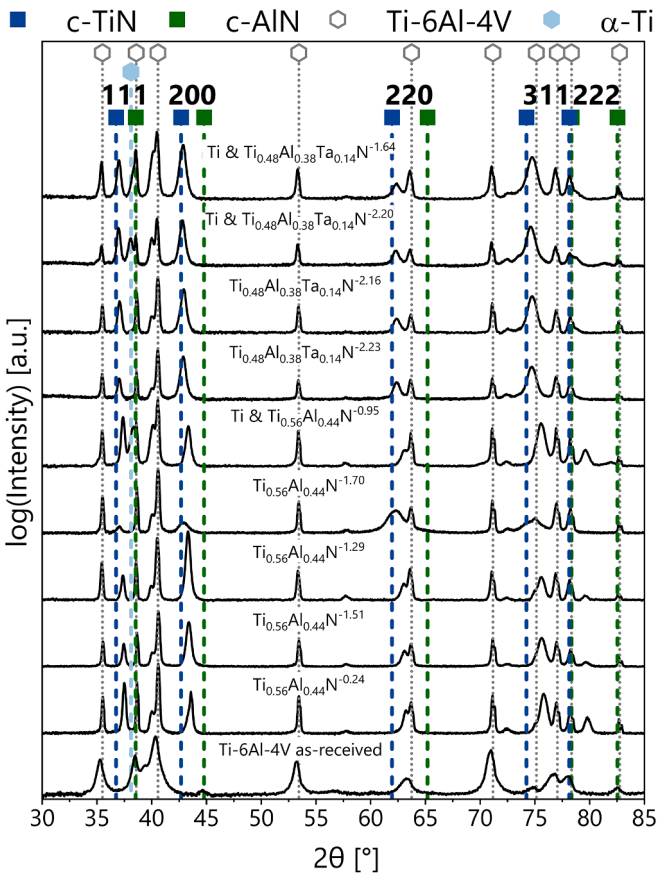

Fig. 2. Bragg-Brentano X-ray diffraction patterns of the as-received Ti-6Al-4V substrate and the investigated coating systems. References taken from [61–64].

literature, the incorporation of the larger Ta atoms into the face-centered cubic crystal lattice resulted in pronounced peak shifts to lower 2θ angles, suggesting uniformly increased lattice parameters and thus higher residual compressive stress [51,59]. Consequently, X-ray stress analysis yields a residual stress in the film plane ($\sigma_{r,\parallel}$) between −1.6 and −2.2 GPa – see Table 1. In comparison, $Ti_{56}Al_{44}N$ deposited at the same bias voltage ($U_S = -40$ V) exhibits $\sigma_{r,\parallel}$ ranging from −1 to −1.5 GPa. Furthermore, the bias variation led to the anticipated residual stress modification. Especially at $U_S = -20$ V, the compressive stress state decreased significantly to -0.24 ± 0.06 GPa. However, for the coating deposited at a bias voltage of −80 V, only a slight additional increase of the residual stress in the film plane to -1.70 ± 0.09 GPa was achieved. Accordingly, the heavier ion bombardment resulted in an imperfect crystal lattice and non-uniform micro-strains, as indicated by the prominent broadening of its XRD peaks [60]. In addition, the introduction of the thin titanium interlayer had a negligible effect on $\sigma_{r,\parallel}$

Table 1
Detailed overview of the residual stress and mechanical properties of the synthesized coatings. From left to right, the following abbreviations are used: Bias voltage (U_S), Residual in-plane stress ($\sigma_{r,\parallel}$), Indentation hardness (H), Young's modulus (E) and Fracture toughness (K_{IC}).

Coating system	U_S[V]	$\sigma_{r,\parallel}$[GPa]	H[GPa]	E[GPa]	H/E[-]	H^3/E^2[GPa]	K_{IC}[MPa$\sqrt{m}$]
$Ti_{0.56}Al_{0.44}N^{-0.24}$	−20	-0.24 ± 0.06	26.09 ± 1.40	406.15 ± 17.93	0.064 ± 0.004	0.11 ± 0.02	–
$Ti_{0.56}Al_{0.44}N^{-1.51}$	−40	-1.51 ± 0.15	26.84 ± 1.83	413.44 ± 13.59	0.065 ± 0.005	0.11 ± 0.02	2.78 ± 0.20
$Ti_{0.56}Al_{0.44}N^{-1.29}$	−40	-1.29 ± 0.13	27.72 ± 1.86	393.53 ± 18.86	0.069 ± 0.006	0.13 ± 0.03	–
$Ti_{0.56}Al_{0.44}N^{-1.70}$	−80	-1.70 ± 0.09	31.35 ± 1.02	397.54 ± 15.11	0.079 ± 0.004	0.20 ± 0.03	–
Ti & $Ti_{0.56}Al_{0.44}N^{-0.95}$	−40	-0.95 ± 0.15	27.76 ± 1.71	438.30 ± 17.83	0.063 ± 0.005	0.11 ± 0.02	2.69 ± 0.10
$Ti_{0.48}Al_{0.38}Ta_{0.14}N^{-2.23}$	−40	-2.23 ± 0.11	27.57 ± 0.71	414.15 ± 18.66	0.067 ± 0.003	0.12 ± 0.02	2.64 ± 0.16
$Ti_{0.48}Al_{0.38}Ta_{0.14}N^{-2.16}$	−40	-2.16 ± 0.17	28.91 ± 2.06	407.92 ± 15.62	0.071 ± 0.006	0.15 ± 0.03	–
Ti & $Ti_{0.48}Al_{0.38}Ta_{0.14}N^{-2.20}$	−40	-2.20 ± 0.18	26.67 ± 1.50	410.13 ± 11.94	0.065 ± 0.004	0.11 ± 0.02	2.52 ± 0.34
Ti & $Ti_{0.48}Al_{0.38}Ta_{0.14}N^{-1.64}$	−40	-1.64 ± 0.14	30.33 ± 1.61	381.30 ± 16.74	0.080 ± 0.005	0.19 ± 0.03	–

of the TiAlN-based top-coating.

Nanoindentation experiments of $Ti_{56}Al_{44}N$ deposited at $U_S = -40$ V confirmed hardness (H) values of about 27 GPa, which is in close agreement to previous studies [65,66]. By increasing the bias voltage to −80 V, a rise in hardness to 31 GPa was observed. In general, this behavior can be attributed to the increased defect formation and slightly enhanced stress state [67]. Furthermore, since the Young's modulus (E) for all $Ti_{56}Al_{44}N$ thin films was found to be approximately 400 GPa (see Table 1), the H/E and H^3/E^2 ratios increased slightly to 0.08 and 0.20 GPa, respectively. According to literature, this may indicate an improved resistance to plastic deformation and improved ductility of the ceramic coating [21]. Nevertheless, this correlation should be interpreted with caution, as it does not account for the influence of plasticity and advanced architecture on coating toughness [68]. Interestingly, the alloying of tantalum had only a minor effect on the mechanical properties. Similar to the ternary coating states, indentation hardness remained around 28 GPa and Young's moduli around 400 GPa for all $Ti_{0.48}Al_{0.38}Ta_{0.14}N$ coatings. As a consequence, the H/E and H^3/E^2 ratios hardly differ from each other (see Table 1). Likewise, the fracture toughness (K_{IC}) evaluated by micro-mechanical cantilever bending tests was barely influenced by the addition of Ta ($K_{IC} = 2.64 \pm 0.16$ MPa$\sqrt{\text{m}}$ for $Ti_{0.48}Al_{0.38}Ta_{0.14}N^{-2.23}$). Contrary to recent studies [49], this fracture toughness value is lower than that observed for the ternary system (2.78 ± 0.20 MPa$\sqrt{\text{m}}$) and quite similar to that found by Bartosik et al. [69], who obtained 2.7 ± 0.3 MPa$\sqrt{\text{m}}$ for $Ti_{40}Al_{60}N$. Therefore, Ta alloying of about 14 % on the metal sublattice did not result in enhanced mechanical properties. As the same overall trend was evident for the interlayer systems, it can be inferred that the introduction of the thin titanium interlayer had a negligible effect on the mechanical properties of the TiAlN-based top coating. A comprehensive summary of all the stress states evaluated by the $sin^2(\psi)$-method as well as mechanical properties obtained from nanoindentation and micromechanical bending experiments is shown in Table 1.

3.2. Fatigue characteristics of uncoated and coated Ti-6Al-4V specimen

In order to provide a reference for the fatigue behavior of the coated specimens, the uncoated fully equiaxed Ti-6Al-4V specimens were tested first. At an applied stress ratio of −1 and a frequency of 10 Hz, the single cantilever experiments resulted in a HCF limit of about 420 MPa. Based on this, the subsequently recorded fatigue properties of the different coating approaches were correlated and presented in the following.

In agreement to Sivagnanam Chandra et al. [14], the variation of the bias voltage and hence stress state caused a significant change in the fatigue life of the hard coated titanium alloy (see Fig. 3**a**). With a HCF strength of 387 MPa, the deposition of $Ti_{0.56}Al_{0.44}N^{-0.24}$ at $U_S = -20$ V yields a decrease of 33 MPa or 8 % in comparison to the uncoated Ti-6Al-4V. Presumably, the residual compressive stress state of the coating ($\sigma_{r,\parallel} = -0.24 \pm 0.06$ GPa) was too low, as each force amplitude (P) caused overall tensile stresses in the thin ceramic film ($\sigma_{K,a,max} + \sigma_{r,\parallel}150\text{MPa} > 0$). As a result, slip step formation at the coating-substrate interface likely contributed to premature coating failure and a diminished HCF strength of the coating-bulk material combination [21]. In addition, the overall tensile stress field increased the coating crack velocity at larger stress amplitudes, which reduced the LCF properties of the underlying titanium alloy.

However, already at a bias voltage of −40 V ($\sigma_{r,\parallel} = -1.29 \pm 0.13$ GPa), the fatigue limit of the coated specimens increases drastically – see green data points in Fig. 3**a**. Compared to the uncoated Ti-6Al-4V fatigue samples, the recorded HCF strength of 508 MPa is an improvement of 88 MPa or 21 %. Furthermore, a shift of the $S-N$ curve to a higher number of load cycles to failure can be observed in the low-cycle regime ($N < 10^5$). For the specimens coated at $U_S = -80$ V ($\sigma_{r,\parallel} = -1.70 \pm 0.09$ GPa), a further improved fatigue behavior is obtained, with the HCF limit found to be 540 MPa (+120 MPa or +29 %). With respect to the

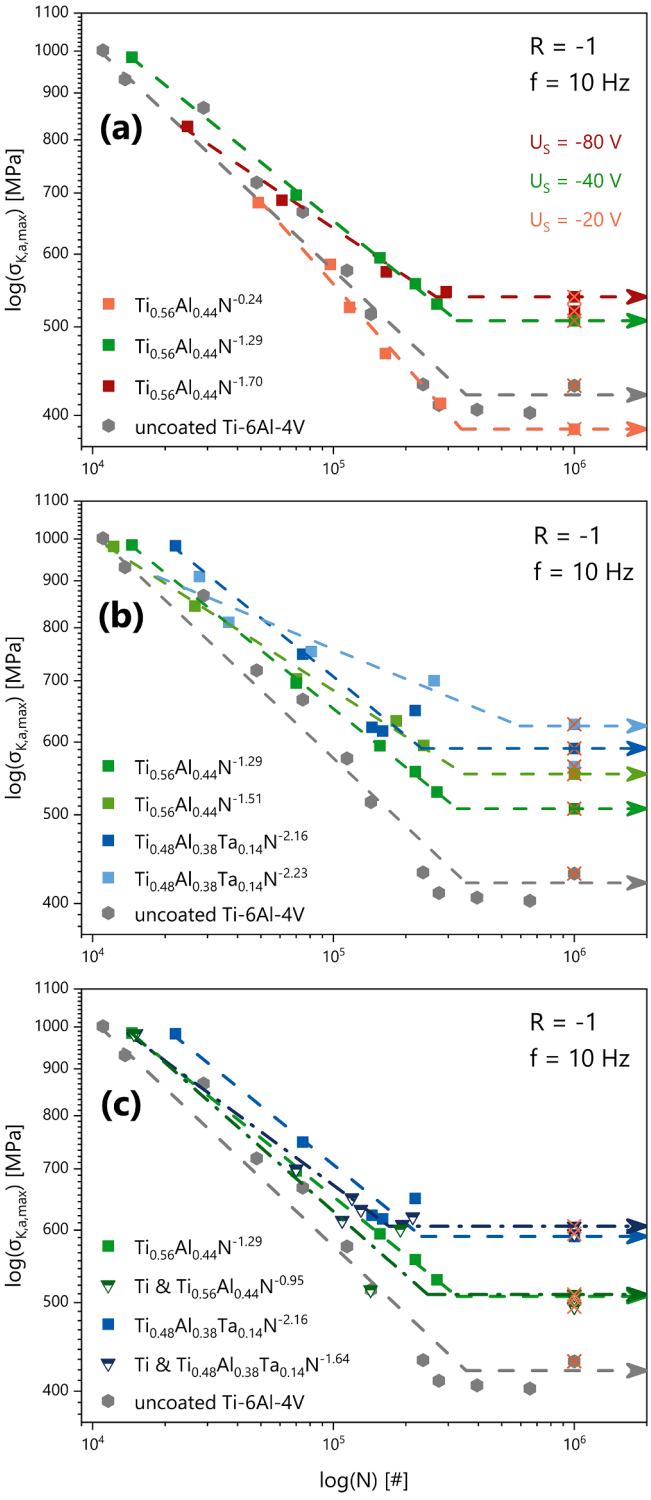

Fig. 3. Fatigue behavior of the different synthesis approaches in relation to the uncoated Ti-6Al-4V fatigue specimen: S −N curves obtained by (a) varying the bias voltage, (b) alloying with tantalum, and (c) introducing a titanium interlayer. High-cycle fatigue tests that reached 10^6 load cycles without failure are marked with a red cross. (For interpretation of the references to colour in this figure legend, the reader is referred to the web version of this article.)

"film induced cracking of substrate" model, it must be assumed that the pronounced residual compressive stress field of $Ti_{0.56}Al_{0.44}N^{-1.29}$ and $Ti_{0.56}Al_{0.44}N^{-1.70}$ successfully prevented film rupture by suppressing strain localization of the cyclically built-up slip bands. Thus, the fatigue

crack nucleation was shifted to the interior of the titanium alloy, where crack initiation is expected to be due to the fracture of brittle α grains. Furthermore, the accumulation of dislocations at the interface leads to a long-range back stress inhibiting the emission of additional dislocations and facilitates the formation of secondary slip systems [21,70]. As a result, the increased compressive stress state of the ceramic coating may not only improve the HCF fatigue properties of the underlying Ti-6Al-4V by changing its fatigue crack initiation mechanism, but also by relieving local stress concentrations at the coating-substrate interface. Thus, the following conclusions emerge: A sufficiently high residual compressive stress state must be present in TiAlN-based coatings ($\sigma_{K,a,max} + \sigma_{r,\parallel} \ll 0$), otherwise its deposition will result in reduced fatigue performance. However, once this condition is met, the higher the residual compressive stress of the thin film, the higher the HCF strength of the material pairing.

Additional evidence of the previously established hypothesis is provided by the fatigue behavior of the $Ti_{0.48}Al_{0.38}Ta_{0.14}N$ coated Ti-6Al-4V specimens (see Fig. 3**b**). As indicated in **section 3.1**, the incorporation of the larger tantalum atoms did not alter mechanical properties but increased residual compressive stress states. Thus, a distinct residual stress-dependent increase in fatigue characteristics emerges. Overall, an improvement of 208 MPa or 50 % compared to the uncoated titanium alloy was recorded for $Ti_{0.48}Al_{0.38}Ta_{0.14}N^{-2.23}$, as the material pairing reached 10^6 load cycles with no noticeable change in strain or stiffness at an applied stress amplitude of 628 MPa. By looking at the $S-N$ curves presented in Fig. 3**c**, the introduction of a ductile titanium interlayer appears to be not further beneficial to the fatigue properties. The coatings with interlayer perform nearly identical to their counterparts without interlayer, but all clearly enhanced compared to the uncoated Ti-6Al-4V specimens.

However, a different trend becomes evident, when the recorded data is examined from a residual stress perspective, see Fig. 4. In comparison to the coating states without an interlayer, an improved relationship between residual stress state and high-cycle fatigue limit emerges — filled squares without interlayer versus semi-filled triangles with interlayer. Consequently, the interlayer systems demonstrate the capacity to withstand greater load amplitudes at reduced residual top-coating stresses. These findings prompt the question: What is responsible for the observed phenomenon? A potential explanation may be provided by

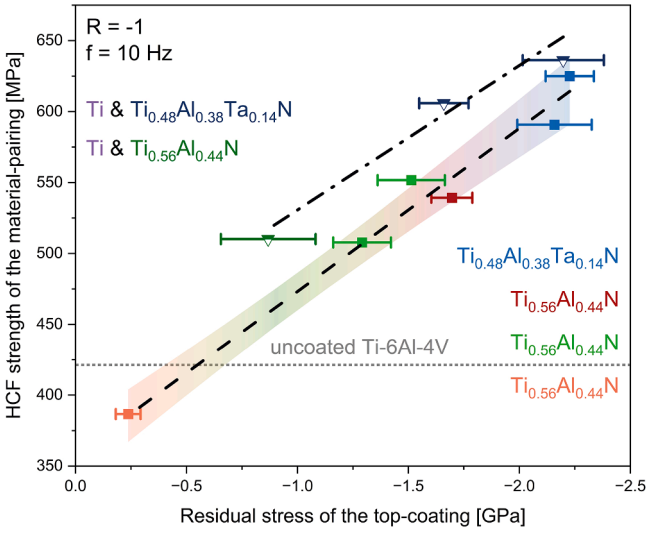

Fig. 4. Effect of the residual stress state of arc evaporated TiAlN thin film systems on the HCF strength (10^6 load cycles) of coated Ti-6Al-4V fatigue specimens. The filled squares represent coating systems without an interlayer, whereas the semi-filled triangles indicate those that include a thin interlayer. For reference, the fatigue limit of the uncoated Ti-6Al-4V specimens is plotted as a dotted line.

Bai et al. [19]. Based on a finite element analysis, they identified a notable reduction in localized stress concentrations at the coating-substrate interface of Cr & TiN coated Ti-6Al-4V compared to coated substrates without the thin Cr interlayer. The authors proposed that the enhanced deformability of the metallic interlayer mitigated the detrimental effects of brittle coating fracture on the underlying Ti-6Al-4V substrate. However, it may be that their top-coating lacked a sufficiently pronounced residual compressive stress state, as physical vapor deposited TiN can exhibit lower average residual compressive stresses than TiAlN [66]. Accordingly, the assumed mechanism cannot explain, how the interlayer improves the fatigue properties, when premature film cracking is successfully prevented (i.e. $\sigma_{K,a,max} + \sigma_{r,\parallel} \ll 0$) and crack nucleation is pushed deep into the interior of the titanium alloy.

3.3. Depth-resolved stress analysis

To assess how the different coating approaches influence the residual stress state of the material pairing, synchrotron X-ray nanodiffraction experiments were performed on coated Ti-6Al-4V substrates. For this purpose, polished cross sections of four selected coating systems were scanned vertically three times with a step size of 100 nm. All investigated states were grown at the same bias potential of −40 V, specifically $Ti_{0.56}Al_{0.44}N^{-1.51}$, Ti & $Ti_{0.56}Al_{0.44}N^{-0.95}$, $Ti_{0.48}Al_{0.38}Ta_{0.14}N^{-2.23}$, and Ti & $Ti_{0.48}Al_{0.38}Ta_{0.14}N^{-2.20}$. Subsequently, the average residual in-plane stress states ($\sigma_{r,\parallel}$) were evaluated and plotted over the height of the sample, with the zero-crossing located exactly at the coating-substrate interface (see Fig. 5).

In summary, all four coating states exhibited more or less constant residual stress states across the thickness of their TiAlN-based top coatings. The discontinuous section of the coating stress profile in Fig. 5**b** is likely caused by macroparticles or evaluation inaccuracies. In addition, the data confirms the anticipated increase in residual compressive stress due to the doping of tantalum: With an average total residual compressive stress of -1.18 ± 0.21 GPa for $Ti_{56}Al_{44}N$ (Fig. 5**a**) and -1.70 ± 0.22 GPa for $Ti_{0.48}Al_{0.38}Ta_{0.14}N$ (Fig. 5**c**), it raises by approximately -0.52 ± 0.31 GPa. This is well within the range of the residual compressive stress increase (-0.72 ± 0.19 GPa) determined by conventional XRD of the same coating states ($Ti_{0.56}Al_{0.44}N^{-1.51}$ and $Ti_{0.48}Al_{0.38}Ta_{0.14}N^{-2.23}$). Nevertheless, slight deviations may occur due to the different geometries and surface conditions of the substrates used: While the conventional XRD stress measurements were performed on the long, narrow and intentionally unpolished Ti-6Al-4V fatigue specimens, the synchrotron X-ray nanodiffraction experiments were carried out on square and polished Ti-6Al-4V substrates. Moreover, it is evident, that the titanium interlayer has little effect on the stress state of the top-coating, as the average residual stress of the TiAlN-based thin film is calculated to be -1.01 ± 0.26 GPa (Ti & $Ti_{0.56}Al_{0.44}N$, Fig. 5**b**) and -2.03 ± 0.22 GPa (Ti & $Ti_{0.48}Al_{0.38}Ta_{0.14}N$, Fig. 5**d**), respectively. However, contrary to expectations, the Ti interlayer itself exhibits a tensile stress field. The residual stress appears to be transferred to the Ti-6Al-4V substrate, where it decreases linearly until a stress-free state is reached (around 1.5 μm away from the interface). In contrast, residual compressive stresses are present at the interface of the coating-substrate pairing without interlayer. As the distance from the interface increases, compressive stresses decrease and tensile stresses are measured. Thus, the thin metallic interlayer clearly causes a significant change in the residual stress profile of the interface near region without affecting the mechanical and residual stress properties of the hard top-coating. This observation raises the question of its origin, and even more importantly, if it relates to the improved relationship between residual stress state and high-cycle fatigue limit of the interlayer systems studied. Thus, possible reasons for the modified residual stress gradient are discussed in the following and correlated with HR-TEM, t-EBSD, and ToF-SIMS investigations. Subsequently, a simple linear-elastic stress-failure model is proposed in subsection 3.4 to explain the enhanced fatigue behavior of

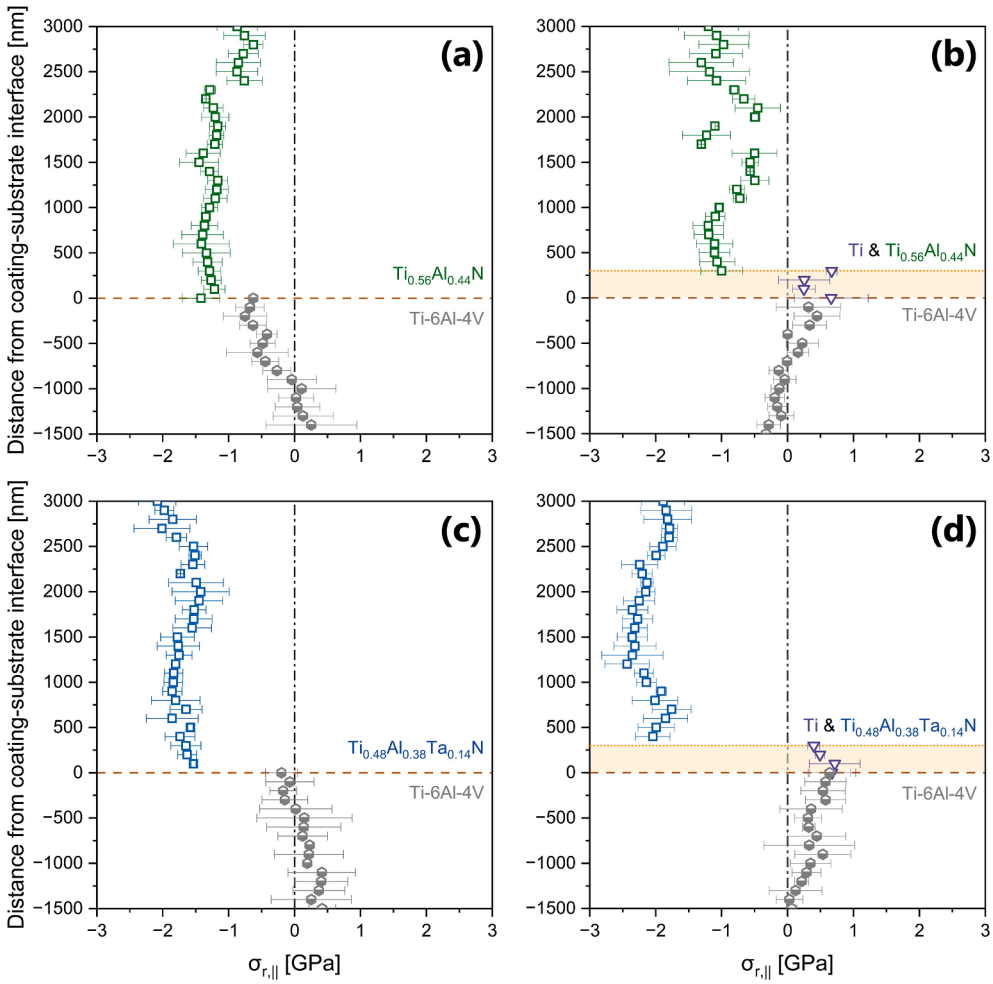

Fig. 5. Residual stress gradients at the coating-substrate interface determined by transmission X-ray nanodiffraction experiments. For comparison purposes, all synchrotron-tested coating systems were synthesized at the same bias voltage: (a) $Ti_{0.56}Al_{0.44}N^{-1.51}$, (b) Ti & $Ti_{0.56}Al_{0.44}N^{-0.95}$, (c) $Ti_{0.48}Al_{0.38}Ta_{0.14}N^{-2.23}$, and (d) Ti & $Ti_{0.48}Al_{0.38}Ta_{0.14}N^{-2.20}$.

the interlayer systems.

In general, the resulting residual stress in a polycrystalline thin-film is determined by a large number of interrelated causes, and their relative contributions typically cannot be disentangled easily. Nevertheless, a distinction is usually made based on their origin in the film evaporation process: Extrinsic residual stress, on the one hand, arises from factors like thermal gradients and processing conditions. Intrinsic residual stress, on the other hand, originates from inherent characteristics of the material, such as lattice defects or phase transformations during film growth [29,71]. The primary source of extrinsic residual stress is due to different coefficients of thermal expansion (CTE) of the film and the substrate. However, since a pure α-Ti interlayer was deposited on an $\alpha+\beta$ titanium alloy and the thermal expansion coefficient of TiAlN coatings at the elevated deposition temperature of 450 °C is only slightly different from that of bulk titanium [72,73], the influence of thermal stresses should play a minor role. Contrary to the general trend of increasing CTE with decreasing grain size [74], Panigrahi et al. [75] additionally reported no significant difference in the expansion coefficient of nanocrystalline titanium compared to its micron-sized counterpart. Thus, the tensile stress field at the coating-substrate interface of the interlayer systems is likely to originate from intrinsic phenomena. Before discussing possible causes, however, it is worth taking a closer look at the growth morphology and grain distribution at the various coating-substrate interfaces (see Fig. 6). Interestingly, both quaternary systems are characterized by a layered chemical contrast. This periodic enrichment of the heavier tantalum is presumably due to the two-folded rotation of the substrates during deposition. Furthermore, the thin titanium interlayer is clearly visible in the HR-TEM bright field images, see Fig. 6**b, d**. Based on the irregular dark and bright areas, an increased defect density and a larger portion of grain boundaries can be assumed. The latter assumption is confirmed by t-EBSD presented in Fig. 7**b**, as the small α titanium grains of the interlayer become visible. Moreover, the t-EBSD analysis reveals different growth morphologies for the Ti interlayer and the TiAlN-based top-coating. While the metallic interlayer is characterized by untextured globular grains, the ceramic coating exhibits much large columnar grains. These grow perpendicular to the coating-substrate interface, with the highest grain density at the site of nucleation (see Fig. 7**a**). It is worth noting that the competitive growth of the TiAlN-based top-coatings results in a fairly uniform top surface. Returning to the question raised earlier, the increased number of grain boundaries of the interlayer could well be responsible for the tensile stress during polycrystalline film growth. According to Ref. [76], the interatomic forces acting at the boundaries tend to close any gaps present, thereby subjecting the neighboring crystallites to tensile stress. However, the pronounced tensile stress field at the coating-substrate interface is more likely the result of crystallite coalescence in the initial stages of the interlayer growth [77]. Assuming a perfect array of hexagonal crystallites growing on the substrate, and ignoring any sliding constraints imposed at the coating-substrate interface during spontaneous coalescence, the upper limit of tensile stress in the film can be estimated by

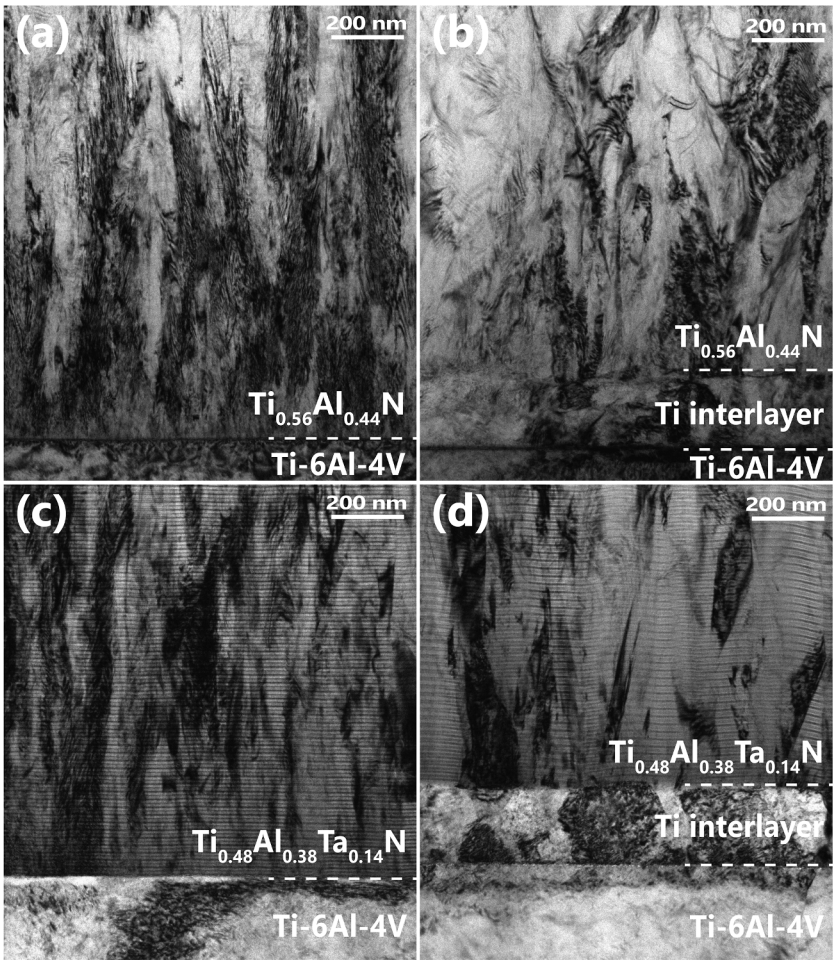

Fig. 6. HR-TEM bright field images of the coating-substrate interfaces, which were studied by transmission X-ray nanodiffraction experiments. The layered structure of the TiAlTaN thin films suggests a periodic enrichment of the heavier tantalum due to the two-folded substrate-rotation during cathodic arc evaporation.

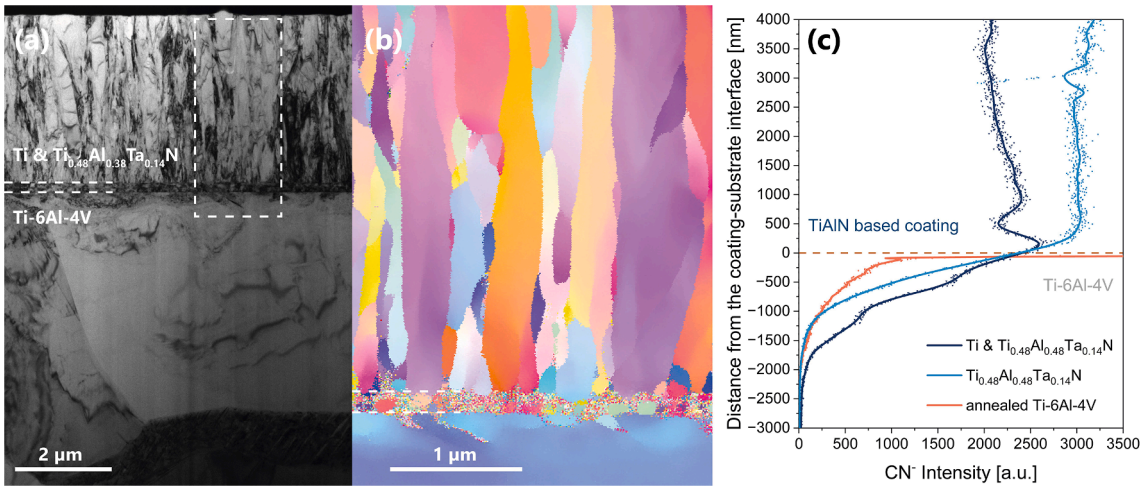

Fig. 7. (a) TEM bright field cross section image of a Ti & $Ti_{0.48}Al_{0.38}Ta_{0.14}N$ coated Ti-6Al-4V substrate. (b) Transmission EBSD image of the area marked in Fig. 7a, revealing the fine-grained morphology of the α titanium interlayer. (c) ToF-SIMS depth profiles of a plasma annealed, a $Ti_{0.48}Al_{0.38}Ta_{0.14}N$, and a Ti & $Ti_{0.48}Al_{0.38}Ta_{0.14}N$ coated Ti-6Al-4V fatigue specimen.

$$\sigma_{max} = \sqrt{\frac{2\gamma_{sv} - \gamma_{gb}}{a}\frac{E}{1-\nu}} \tag{12}$$

where γ_{sv} and γ_{gb} represents interfacial energies and $\frac{E}{1-\nu}$ the biaxial modulus of the elastically isotropic crystallites [78]. By taking characteristic values for our Ti interlayer ($E_{Ti} = 110$ GPa [47], $\nu_{Ti} = 0.32$ [47], $\gamma_{sv,Ti} = 2.6\ \mathrm{Jm}^{-2}$ [79], $\gamma_{gb,Ti} = 1\ \mathrm{Jm}^{-2}$ [80]) and an average grain size of $2a = 150$ nm, the maximum tensile stress is found to be $\sigma_{max} = 3.01$

GPa. Seel et al. [81] confirmed the tensile stress generation during coalescence-grain boundary zipping. However, using finite element simulations, they found that the Nix-Clemens model [78] generally leads to an overestimation. Thus, they predicted smaller stress values, which is more consistent with our experimentally measured interface tensile stress state, as shown in Fig. 5**b, d**. In addition, the high melting point of Ti leads to strongly reduced atomic mobility, which limits stress relaxation and results in more persistent tensile stresses during subsequent film growth [82,83]. Yet, it is important to note that the monochromatic X-ray beam can only be focused to a probe cross section of approximately 250 nm. Combined with the fact that our Ti-6Al-4V substrate produces the same diffraction patterns as our Ti interlayer, the quantitative stress evaluation of the interlayer must therefore be treated with caution.

Nevertheless, transmission X-ray nanodiffraction measurements clearly indicate that the deposition of the 300 nm thick Ti layer modified the stress gradient at the subsurface of the underlying Ti-6Al-4V (see Fig. 5). As described earlier, in contrast to the residual tensile stressed interface of the interlayer system, residual compressive stresses are present at the subsurface of the coating-substrate pairing without interlayer. A possible explanation for this behavior may be, that the Ti interlayer acts as a diffusion barrier during the reactive deposition process. In the absence of a metallic interlayer, nitrogen atoms can diffuse into the activated near-surface region of the Ti-6Al-4V bulk material, where they are usually incorporated at interstitial positions of the crystal, which could explain the observed residual compressive stress field [84]. However, the ToF-SIMS depth profiles of a plasma annealed, a $Ti_{0.48}Al_{0.38}Ta_{0.14}N$, and a Ti & $Ti_{0.48}Al_{0.38}Ta_{0.14}N$ coated Ti-6Al-4V fatigue specimen revealed that the CN^- signal drops rapidly at the interface in all cases (see Fig. 7**c**). Although the interfaces are further roughened by the gradual material removal during the ToF-SIMS sputtering process, which may limit the precision of the depth scale, the common trend is clearly visible. Therefore, the near-surface region of the Ti-6Al-4V substrate was not nitrided during the deposition process. Thus, the Ti interlayer did not act as a diffusion barrier. Presumably, the tensile stress field within the interlayer is transmitted across the coating-substrate interface in a strain-based manner. As the distance from the interface increases, the induced lattice compressions gradually decrease until they reach equilibrium at a certain depth. However, additional experiments are needed to fully understand the intrinsic origin and underlying mechanisms of the altered residual stress gradient.

4. Discussion

As outlined in section 3.2, once a sufficiently pronounced residual compressive stress is present in the TiAlN-based top-coating ($\sigma_{K,a,max} + \sigma_{r,\|} \ll 0$), the HCF strength of the material pairing improves in comparison to the uncoated substrate. Regarding the "film induced substrate cracking" model, the fatigue crack nucleation is thereby shifted to the interior of the titanium alloy, where crack initiation is related to fracture of brittle α grains. According to Ref. [21], the deposition of a TiN/AlN superlattice coating enhanced the fatigue properties by pushing the crack source 50 to 250 μm into the Ti-6Al-4V substrate. Although not discussed in their work, it is worth noting that such multilayer coatings can easily achieve average residual compressive stresses of up to −4 GPa owing to their two-layer periodicity in the nanometer range [85–88]. Therefore, it seems reasonable to assume that the high residual stress state of the TiN/AlN superlattice coating caused the observed shift of crack nucleation. Let's now additionally consider that the residual stresses of coated substrates must always obey macroscopic equilibrium conditions, i.e., the forces and moments associated with them must be compensated over depth. It becomes clear that the compressive stress gradient in the thin film leads to a tensile stress peak in the substrate [29]. Combined with the cyclically applied load, the tensile stress field inside the Ti-6Al-4V bulk material can ultimately activate dislocation motion in the available slip planes. Since plastic deformation in the hexagonal closed packed α grains is severely restricted in contrast to the body centered cubic β phase, fatigue cracks initiate along slip bands within the α grains for fully equiaxed microstructures [89]. Consequently, not only the improvement of the compressive stress state of the top-coating, but also the modification of the residual tensile stress state in the subsurface seems to be of paramount importance for the HCF behavior of hard coated Ti-6Al-4V.

In this regard, valuable insights are provided by a numerical study by Baragetti et al. [90], who investigated the relationship between fatigue behavior and stress gradients of notched and smooth TiN coated Ti-6Al-4V specimens. After conducting fatigue experiments, a three-dimensional finite element model was used to gain a deeper understanding. Interestingly, the simulated deposition process led to similar residual stress profiles for both geometries: Under loading conditions, the total subsurface tensile stress peaked at a distance of 30 to 80 μm from the coating surface. Based on fracture surface analysis of coated specimens, the numerical maximum tensile stress field was finally correlated with fatigue crack initiation. As a result, the researchers concluded that the application of physically vapor deposited nitride coatings can inhibit surface crack initiation and trigger subsurface crack nucleation in the area of the maximum tensile stresses. Apart from this study, however, the influence of residual tensile stresses in the bulk material has generally been overlooked, as recently noted by Zhang et al. [16]. To address this shortcoming and analytically study the resulting residual stress gradient within the Ti-6Al-4V substrate, the recorded stress gradients and fatigue properties of the material pairing have been incorporated into a simple linear-elastic stress-failure model.

4.1. Experimental foundation of linear-elastic stress-failure model

In a first step, the residual stress gradients of $Ti_{0.48}Al_{0.38}Ta_{0.14}N^{-2.23}$, Ti & $Ti_{0.48}Al_{0.38}Ta_{0.14}N^{-2.20}$ and Ti & $Ti_{0.56}Al_{0.44}N^{-0.95}$ were evaluated over larger depths into the substrate. Fig. 8 clearly shows, that the thin Ti interlayer alters the residual stress gradient of the Ti-6Al-4V specimen. For the coating-substrate pairing without interlayer, residual compressive stresses are present at the interface. As the distance from the interface increases, the compressive stresses decrease, so that slight tensile stresses (oscillating around zero) are observed at a depth of −8000 nm (see Fig. 8**a**). In contrast, the residual tensile stress state of the interlayer seems to be transferred at the coating-substrate interface in a strain-based manner. Subsequently, the stresses decrease linearly, so that residual compressive stresses are present beyond a depth of approximately −1000 to −2000 nm. Compared to Ti & $Ti_{0.56}Al_{0.44}N$ (Fig. 8**c**), the Ti & $Ti_{0.48}Al_{0.38}Ta_{0.14}N$ (Fig. 8**b**) coated specimen achieves higher compressive stress values on average. Presumably, this is due to the more pronounced residual compressive stress state of the $Ti_{0.48}Al_{0.38}Ta_{0.14}N$ top-coating, as their mean values differ by about -1.03 ± 0.34 GPa (see Fig. 8**b, c**).

Subsequently, the material response of TiAlN coated Ti-6Al-4V to a static load was investigated with the objective of determining whether the deformations could be described by linear-elastic computations. Accordingly, the coating-substrate interface surrounding the pre-notch position of the 24 μm thick microcantilever was studied in detail both before and during in-situ loading. The resulting in-plane stress maps for each loading scenario are given in Fig. 9. In the unloaded state, the $Ti_{0.56}Al_{0.44}N$ coating grown at −120 V bias potential, exhibits nearly constant residual compressive stresses with an average value of $\overline{\sigma_{(r,\|)}} = -3.43 \pm 0.15$ GPa. In contrast to the previously discussed results of the unloaded cross sections, however, pronounced tensile stresses are present in the Ti-6Al-4V substrate within the first 4 μm from the interface ($\overline{\sigma_{(r,\|)}} = 0.62 \pm 0.17$ GPa). By considering the reduced ratio of substrate to coating thickness, it becomes evident that a much faster transition from compressive to tensile stresses is to be expected, given that the overall residual stresses should again be fully relaxed. Furthermore, it is important to note that no coating delamination was

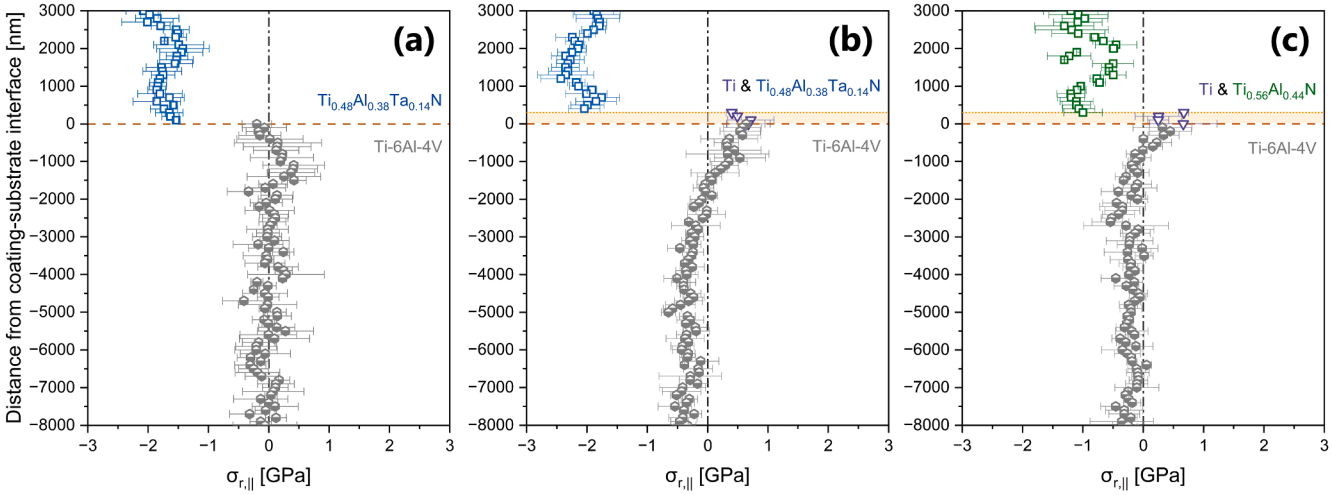

Fig. 8. Depth resolved stress profiles of TiAlN coated Ti-6Al-4V specimen. Each cross section was scanned 8000 nm deep into the titanium alloy using a monochromatic high-energy X-ray beam ($\lambda = 0.6294$ Å) at the nanofocus endstation of beamline P03, PETRA-III, DESY.

observed. This suggests that the residual stresses at the interface did not undergo the presented abrupt change of sign (see Fig. 9**a**). A continuous transition is the more probable scenario, although it cannot be resolved due to the beam diameter of approximately 250 nm. Nevertheless, loading the microcantilever with 10 mN (Fig. 9**b**) and 20 mN (Fig. 9**c**) results in a significant compressive stress reduction in the upper section of the coating. To identify and isolate the impact of the static load application, the unloaded stress distributions were subtracted from the loaded ones, thereby deriving the relative change in the in-plane stress state. In addition, the row-average of the stress data corresponding to comparable vertical positions on the cantilever cross section was calculated (see Fig. 9**d**). The data shows a linear change of the in-plane stress state across the investigated region, with a notable discontinuity at the coating-substrate interface. To enable the evaluation of the experimental outcomes, the linear-elastic stress gradients for both load cases were calculated analytically. Assuming isotropic material behavior and the validity of the Bernoulli hypotheses, the position of the neutral fiber (z_0) can be calculated as follows

$$F_n = \int \sigma(z)dA = \int E(z)\varepsilon(z)dA = \int E(z)\frac{z - z_0}{\rho}dA = 0 \tag{13}$$

$$\rightarrow z_0 = \frac{\sum_i E_i z_{s,i} A_i}{\sum_i E_i A_i} \tag{14}$$

with E_i representing the Young's modulus, A_i the area, and $z_{s,i}$ the distance between the center of gravity and the reference axis of the material section being considered. Subsequently, the linear-elastic stress gradient ($\sigma(z)$) is given by applying the principle of moment equilibrium to the beam cross section

$$M = \int \sigma(z)dA = \int E(z)\frac{z - z_0}{\rho}dA = F_q l \tag{15}$$

$$\rightarrow \sigma(z) = E(z)(z - z_0)\frac{F_{max} l}{\sum_i E_i I_i - z_0 \sum_i E_i z_{s,i} A_i} \tag{16}$$

where F_{max} is the maximum bending load applied, l signifies the length between the pre-notch and the indenter tip, and I_i denotes the area moment of inertia of the examined material section. The resulting calculated stress profiles of a TiAlN coated Ti-6Al-4V cantilever under identical loading conditions is depicted in Fig. 9**e**. In general, the analytically determined stress gradients are found to be in excellent agreement with the experimental ones. As the neutral fiber is solely a function of the cantilever's geometry and material combination (see Eq. (14)), it is situated in both loading cases at a depth of approximately 4 μm within the titanium alloy. Thereafter, tensile stresses increase linearly, until the coating-substrate interface is reached, at which point a discontinuity is observed once again. By looking at Eq. (16), it becomes evident that this phenomenon is a consequence of the mismatch in elastic modulus between the materials involved. Therefore, returning to the objective of this experiment, testing at this reduced length scale has clearly demonstrated that even at elevated stress peak values of about 1 GPa in the outermost fiber, the nitride coated titanium alloy exhibits purely elastic deformation. Consequently, the linear theory of elasticity is an appropriate framework for describing the applied stress gradients of the single-cantilever fatigue tests, which exhibit peak stress values below 1 GPa, and thus for establishing the stress-failure model.

4.2. *Mathematical formulation and constraint-based solution*

As stated in the beginning of Section 4, the maximum residual tensile stress peak within the substrate can serve as a nucleation site for dislocation motion along slip planes, thereby initiating subsurface fatigue cracking under cyclic loading. Yet, the farther this tensile peak is located within the Ti-6Al-4V bulk material, the smaller the contribution of the applied stress amplitude, which always reaches its maximum in the outermost fiber of the specimen (see Fig. 9**e**). Thus, a deeper tensile peak within the substrate should result in an improved fatigue performance, as it requires higher applied forces to initiate dislocation motion and ultimately trigger fatigue failure. To test this hypothesis and evaluate how different residual stress designs influence the fatigue-critical stress distribution, it is essential to track the position of the residual tensile stress peak within the substrate.

Therefore, the general objective of the linear-elastic stress-failure model is to derive the complete residual stress gradient as a function of the experimentally determined near-surface residual stress state and its investigated relation to the fatigue properties of TiAlN coated Ti-6Al-4V. Overall, it incorporates two input variables: *(i)* the residual stress state of the top-coating and *(ii)* whether an interlayer is present or not (represented as "No Interlayer system" and "Interlayer system" in the equality constraints). In order to establish a link between coating stress and fatigue specimen failure, the residual compressive stress of the top-coating is correlated with the recorded high-cycle fatigue strength of the material combination. Consequently, the relationship depicted in Fig. 4 is linearly approximated for both interlayer and non-interlayer coating systems. Given that each top-coating stress state ($\sigma_{r,||}$) is now associated with an applied stress peak in the outermost fiber of the notched specimen ($\sigma_{K,a,max}$), it is possible to calculate the related applied stress

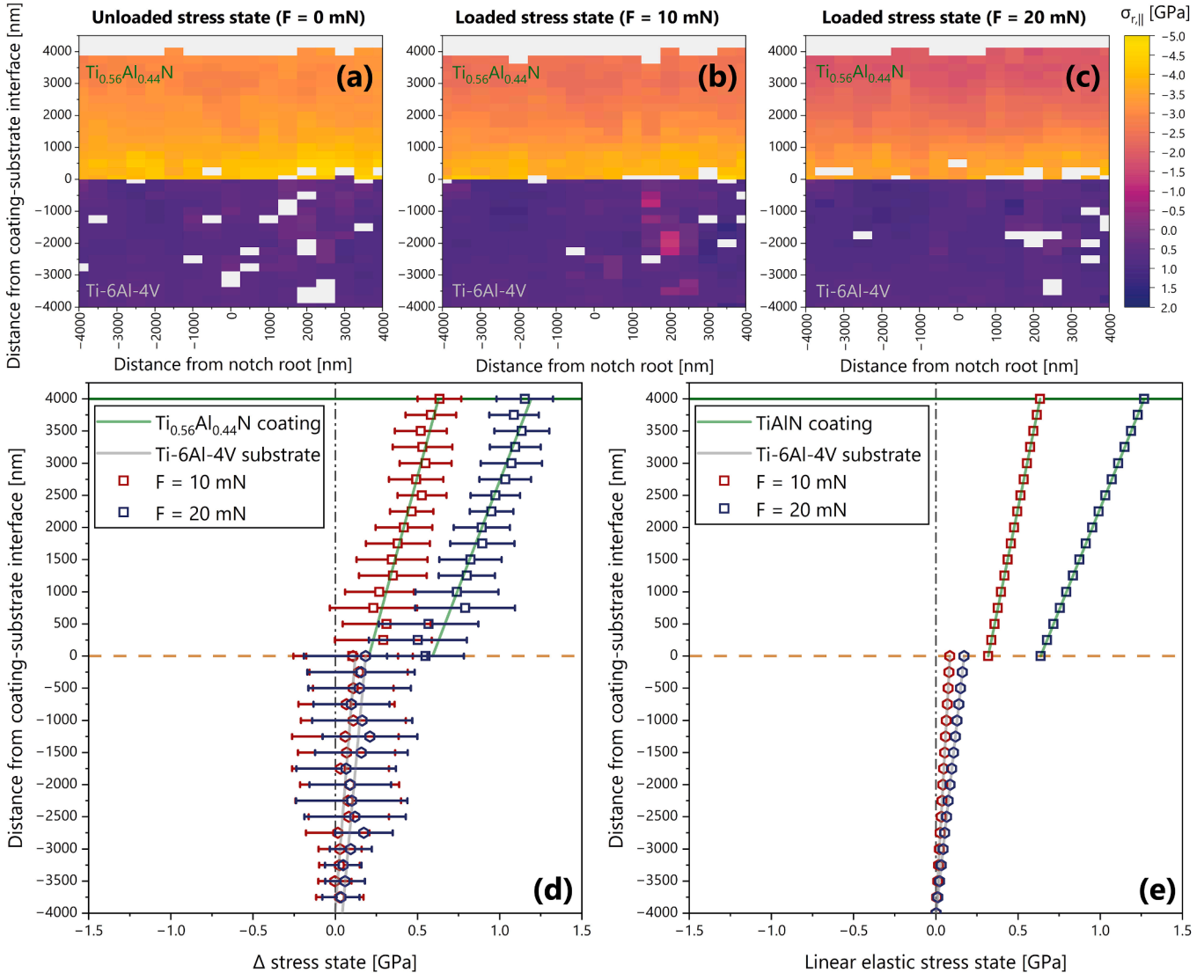

Fig. 9. Experimental and analytical in-plane stress response of a TiAlN coated Ti-6Al-4V microcantilever subjected to static load conditions. For the experimental stress analysis, an array of 40 × 16 diffraction scans were conducted along the Z- and Y-axes, with the center located at the notch root of the cantilever. Overall stress map at the interface of the (a) unloaded, (b) 10 mN and (c) 20 mN loaded microcantilever. (d) Corresponding cross-sectional row-average of the difference between the experimentally obtained loaded and unloaded stress data. (e) Analytically determined linear-elastic stress gradient of a Euler-Bernoulli cantilever beam with the same properties as the studied microcantilever.

gradient ($\sigma_{K,a}(z)$) using linear elastic computations. This stress gradient is a close estimate to that at which fatigue failure should occur for the specific coating-substrate pairing during the single cantilever fatigue testing. In general, the applied stress gradient ($\sigma_{K,a}(z)$) peaks in the outermost fiber and decreases linearly until it reaches zero at the axis of symmetry of the specimen. We define this stress-free axis as the "neutral fiber" and the origin of the model's coordinate system, thereby dividing the specimen into two symmetric halve. Since each custom-made fatigue specimen is coated evenly on all sides, the coating starts in the model at $\pm\frac{h_s}{2} = \pm 350$ µm. Due to the fully reversed loading condition ($R = -1$), each half of the specimen alternately experiences compressive and tensile stress with each load cycle. Thus, both the geometry and loading conditions are symmetric and only one half of the coated substrate is considered from this point onward.

In accordance with the numerical study by Baragetti et al. [90], a parabolic stress profile

$$f(z) = az^2 + bz + c \text{ [GPa] } for\ 0 \le z_2 < z < z_1 \le 350 \text{ [µm]} \tag{17}$$

is assumed for the unmeasured part of the Ti-6Al-4V substrate. However, the subsurface region is modeled based on the varying stress gradient characteristics observed via transmission X-ray nanodiffraction measurements, which have been extensively discussed throughout this work. As a result, five unknowns (a, b, c, z_1 and z_2) remain, which are solved using the following five equality constraints:

$$\text{I} : \epsilon_c\left(\frac{h_s}{2}\right) = \epsilon_s\left(\frac{h_s}{2}\right) \ldots \text{No Interlayer system} \tag{18}$$

$$\text{II} : z_1 = \frac{h_s}{2} \ldots \text{No Interlayer system} \tag{19}$$

$$\text{I} : f(z_1) = 0.2\sigma_c \ldots \text{Interlayer system} \tag{20}$$

$$\text{II} : z_1 = \frac{h}{2} - 10 \ldots \text{Interlayer system} \tag{21}$$

$$\text{III} : \int_{z_1}^{z_2} f(z)dz = \int_{\frac{h_s}{2}+h_c}^{z_1} \sigma_{r,\|}(z)dz \ldots \text{Both systems} \tag{22}$$

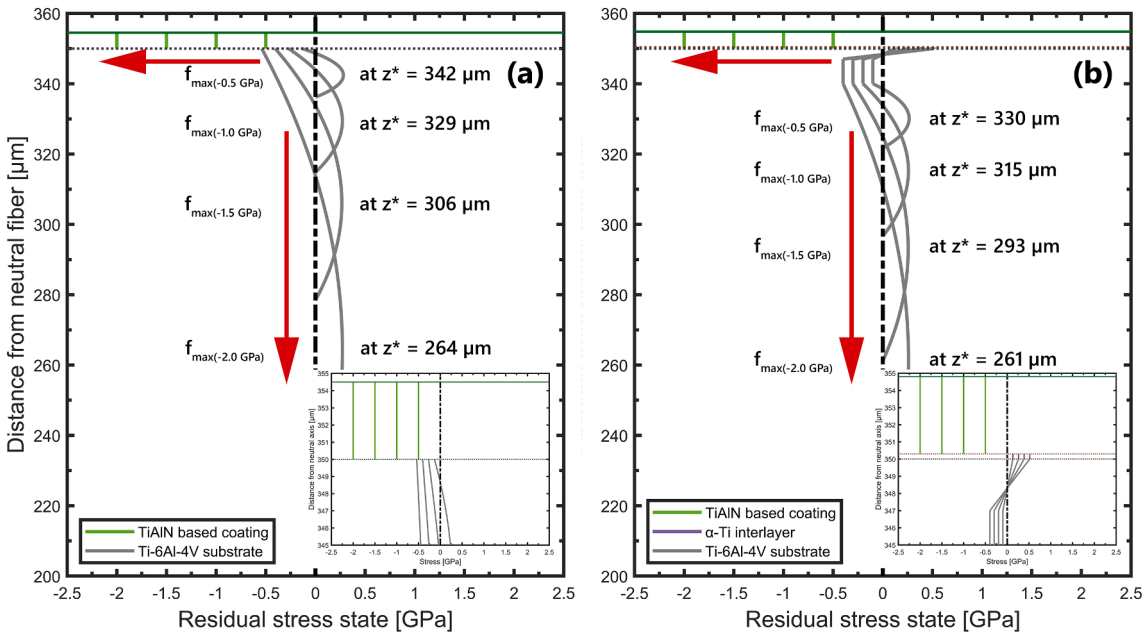

Fig. 10. Resulting residual stress gradients within the substrate for four different TiAlN top-coating stress states ($\sigma_{r,\|} = -0.5,\ -1.0,\ -1.5$ and -2.0 GPa, respectively, indicated by vertical green lines): (a) without ("No Interlayer system") and (b) with a thin α titanium interlayer ("Interlayer system"), determined by the linear-elastic stress-failure model. The neutral fiber (where $\sigma_{K,a}(z) = 0$) defines the origin of the model's coordinate system. Insets in subplots (a) and (b) show magnified views of the residual stress gradient at the coating–substrate interface, altered by residual stress design. (For interpretation of the references to colour in this figure legend, the reader is referred to the web version of this article.)

$$\mathrm{IV}: f(z^*) + \sigma_{K,a}(z^*) = \xi_{0,prism} \ \ldots \text{Both systems} \tag{23}$$

$$\mathrm{V}: f(z_2) = 0 \ \ldots \text{Both systems} \tag{24}$$

For the coated titanium substrates without interlayer, equal coating and substrate strain at the interface is assumed to prevent plastic deformation or delamination ($\mathrm{I}: \epsilon_c(\frac{h_s}{2}) = \epsilon_s(\frac{h_s}{2})$). Furthermore, the parabolic stress gradient starts directly at the boundary between coating and substrate ($\mathrm{II}: z_1 = \frac{h_s}{2} = 350$ µm). In contrast, the interlayer systems are characterized by a tensile stress field at the interface and a compressive stress field in the subsurface (see Fig. 8). Synchrotron based experiments have shown, that these compressive stress values increase as the residual compressive stress state of the top-coating becomes more pronounced. Therefore, this trend is accounted for in the first 10 µm of the residual stress profile. After that, the parabolic stress gradient sets in ($\mathrm{I}: f(z_1) = 0.2\sigma_c$, $\mathrm{II}: z_1 = \frac{h_s}{2} - 10 = 340$ µm). For both systems, however, the size and shape of the stress gradient is defined by the same constraints. First, the parabolic stress profile must balance all residual stress states of the thin film to achieve macroscopic equilibrium ($\mathrm{III}: \int_{z_1}^{z_2} f(z)dz = \int_{\frac{h_s}{2}+h_c}^{z_1} \sigma_{r,\|}(z)dz$). Furthermore, the residual tensile stress field inside of the fully equiaxed Ti-6Al-4V substrate should exactly be able to initiate plastic deformation during high-cycle fatigue experiments. Research has demonstrated that at the onset of plasticity, three distinct slip families can be active in the α phase of titanium alloys [91]. Of these, prismatic slip exhibits the lowest initial critical resolved shear stress ($\xi_{0,prism}$), making it the most favorable plane for dislocation movement [92,93]. Accordingly, once the combined stress value reaches this threshold, it can theoretically be assumed that dislocation motion starts and fatigue crack initiation occurs. In the context of the linear-elastic stress-failure model, the combined stress value is defined as the sum of the tensile stress peak of the parabolic stress gradient ($f(z^*) with \frac{\partial f(z^*)}{\partial z} = 0$) and the linear elastic applied stress state at the location of the peak ($\sigma_{K,a}(z^*)$). It is crucial to highlight again that the parabolic stress profile ($f(z)$), which is calculated for a specific top-coating stress state, is superimposed with the applied stress gradient ($\sigma_{K,a}(z)$), which is consistent with the empirical trend observed in Fig. 4. In light of these considerations, the equality constraint is expressed in the form of $\mathrm{IV}: f(z^*) + \sigma_{K,a}(z^*) = \xi_{0,prism} = 0.39$ GPa. Finally, the parabolic stress gradient must reach an unstressed state once all conditions are fulfilled ($\mathrm{V}: f(z_2) = 0$).

Assuming that premature coating failure is effectively suppressed by the sufficiently pronounced residual compressive stress state of the TiAlN-based top-coating (i.e., $\sigma_{K,a,max} + \sigma_{r,\|} \ll 0$), the linear-elastic stress–failure model reveals the following trend: The greater the compressive stress state of the ceramic coating, the deeper the tensile stress peak of the parabolic stress gradient is shifted into the interior of the titanium alloy. This behavior is clearly evident in Fig. 10**a**, which displays the residual stress gradients of TiAlN coated Ti-6Al-4V fatigue specimens subjected to four different thin film stress states indicated by vertical green lines ($\sigma_{r,\|} = -0.5,\ -1.0,\ -1.5$ and -2.0 GPa, respectively). Each film stress state results in a different location of the tensile stress peak within the substrate, denoted by z^*. A coating stress state of $\sigma_{r,\|} = -0.5$ GPa shifts the peak by only 8 µm, whereas an elevated compressive stress state of -2 GPa pushes it as far as 86 µm away from the coating-substrate interface (i.e., $\frac{h_s}{2} - z^*$). Thereby, it increases the material's tolerance to applied stress, as higher external loads are required to reach the critical resolved shear stress in the substrate and ultimately initiate fatigue failure.

By comparing these results with the residual gradients of the Ti & TiAlN coated Ti-6Al-4V specimens shown in Fig. 10**b**, it becomes evident that adapting the stress state at the interface significantly affects the location of the tensile stress peak within the bulk material. This effect seems to be particularly pronounced at lower residual compressive stress levels in the top-coating, as the incorporation of a thin Ti interlayer leads to a deeper positioning of the tensile stress peak compared to specimens without an interlayer, despite exhibiting the same film stress states. For instance, a coating stress state of $\sigma_{r,\|} = -1$ GPa results in a peak shift of 21 µm for a TiAlN-coated specimen (see Fig. 10**a**), whereas the addition of a tensile-stressed Ti interlayer increases this distance to 35 µm from the coating–substrate interface (see Fig. 10**b**). Furthermore, a

comparison between $Ti_{0.56}Al_{0.44}N^{-1.29}$ and Ti & $Ti_{0.56}Al_{0.44}N^{-0.95}$ reveals that both configurations result in tensile stress peaks located approximately 33 μm from coating–substrate interface, despite the top-coating stress state of the interlayer system being reduced by nearly 0.35 GPa compared to the system without an interlayer. This is in good accordance with the recorded fatigue data, as both coating states exhibited comparable HCF properties (see Fig. 3**c**). Yet, this effect appears to diminish with increasing stress state in the top-coating. For $\sigma_{r,\|} = -2.0$ GPa, the crack nucleation is found for both systems at about 260 μm from the neutral fiber (see Fig. 10**a and b**).

Overall, the linear-elastic stress-failure model clearly demonstrates that modifying the location of the resulting residual tensile stress peak within the substrate is key to improving the high cycle fatigue strength of TiAlN-based coated Ti-6Al-4V. Accordingly, the altered substrate stress gradient appears to be responsible for the experimentally observed ability of interlayer systems to sustain higher load amplitudes under lower residual compressive stresses in the top-coating. Thus, interlayer-based residual stress design strategies offer a valuable alternative to excessively increasing the residual compressive stress state in the top-coating — which can be problematic due to risks such as coating delamination, buckling, or blistering and may sometimes be infeasible due to the constraints and performance requirements of the material system [67,71,94] — to effectively enhance the HCF performance of ceramic coated titanium alloys.

5. Conclusion

The assessment of the physical, chemical, and mechanical properties of stress-altered coating states clearly demonstrates that the fatigue characteristics of hard coated Ti-6Al-4V are predominantly influenced by the residual stresses present in the TiAlN-based thin films. In addition, the study emphasizes the critical importance of residual stress design for further enhancing the HCF strength of ceramic coated metal substrates. For the first time, it was successfully demonstrated, that the implementation of a thin Ti interlayer resulted in a beneficial modification of the residual stress gradient at the coating-substrate interface. Overall, the deposition of a 4500 nm thick Ti & $Ti_{0.48}Al_{0.38}Ta_{0.14}N^{-2.20}$ coating resulted in an improvement of 216 MPa or 51 % compared to the uncoated Ti-6Al-4V fatigue specimen. Thus, the following conclusions emerge:

1) A sufficiently pronounced residual compressive stress state must be present in the TiAlN-based top-coating ($\sigma_{K,a,max} + \sigma_{r,\|} \ll 0$), otherwise its deposition will result in reduced fatigue performance. Presumably, as soon as each load cycle causes overall tensile stresses in the thin ceramic film ($\sigma_{K,a,max} + \sigma_{r,\|} > 0$), slip step formation at the coating-substrate interface leads to premature coating failure. Subsequently, notch effects induce further stresses on the interface near region, promoting subsurface crack initiation and a diminished HCF strength of the material combination.
2) Once the residual compressive stress field of the TiAlN-based top-coating is able to suppress the formation of cyclically built-up slip bands ($\sigma_{K,a,max} + \sigma_{r,\|} \ll 0$), fatigue crack nucleation is shifted into the interior of the titanium alloy, resulting in enhanced HCF properties.
3) The incorporation of high-brilliance resolved stress profiles into a simple linear-elastic stress-failure model revealed, that the deeper the residual tensile stress peak is shifted into the bulk material, the greater the HCF strength improvement.
4) Finally, the introduction of a tensile stressed titanium interlayer at the coating-substrate interface causes tensile stresses in the first 1 to 2 μm of the bulk material, followed by a pronounced compressive stress field. As a consequence of the altered stress gradient, the residual stress-dependent HCF performance of TiAlN coated Ti-6Al-4V additionally improves, circumventing the need to push compressive stress levels in the top-coating to their limits.

In conclusion, the study not only resolves previous contradictory findings regarding the detrimental versus beneficial effects of hard ceramic coatings on fatigue performance but also establishes clear criteria for optimizing coating design. In particular, it demonstrates that an optimized residual stress distribution, achieved through controlled process parameters and an appropriate interlayer design, is key to utilizing the potential of TiAlN-based coatings to extend the service life of Ti-6Al-4V components.

CRediT authorship contribution statement

A. Gitschthaler: Software, Visualization, Data curation, Writing – original draft, Investigation, Conceptualization, Writing – review & editing, Project administration, Formal analysis, Methodology. **R. Hahn:** Supervision, Funding acquisition, Validation, Writing – review & editing, Investigation. **L. Zauner:** Investigation, Writing – review & editing, Software, Supervision. **T. Wojcik:** Investigation. **F. Fahrnberger:** Investigation, Writing – review & editing. **H. Hutter:** Resources. **A. Davydok:** Investigation, Resources. **C. Krywka:** Resources. **C. Jerg:** Resources. **J. Ramm:** Resources, Writing – review & editing. **A. Eriksson:** Resources, Writing – review & editing. **S. Kolozsvári:** Resources. **P. Polcik:** Resources. **H. Riedl:** Supervision, Funding acquisition, Resources, Methodology, Writing – review & editing, Project administration, Validation.

Declaration of competing interest

The authors declare that they have no known competing financial interests or personal relationships that could have appeared to influence the work reported in this paper.

Acknowledgments

The financial support by the Austrian Federal Ministry for Digital and Economic Affairs, the National Foundation for Research, Technology and Development and the Christian Doppler Research Association is gratefully acknowledged (Christian Doppler Laboratory “Surface Engineering of high-performance Components”). We also thank for the financial support of Plansee SE, Plansee Composite Materials GmbH, and Oerlikon Balzers, Oerlikon Surface Solutions AG. In addition, we want to thank the X-ray center (XRC) of TU Wien for beam time as well as the electron microscopy center — USTEM TU Wien — for providing the TEM facilities. We acknowledge DESY (Hamburg, Germany), a member of the Helmholtz Association HGF, for the provision of experimental facilities. Parts of this research were carried out at PETRA III using the nanofocus endstation of beamline P03. Beamtime was allocated for proposal I-20211636 EC and I-20221274 EC. The authors acknowledge the TU Wien Bibliothek for financial support through its Open Access Funding Programme.

Data availability statement

The data that support the findings of this study are available from the corresponding author upon reasonable request.

Appendix

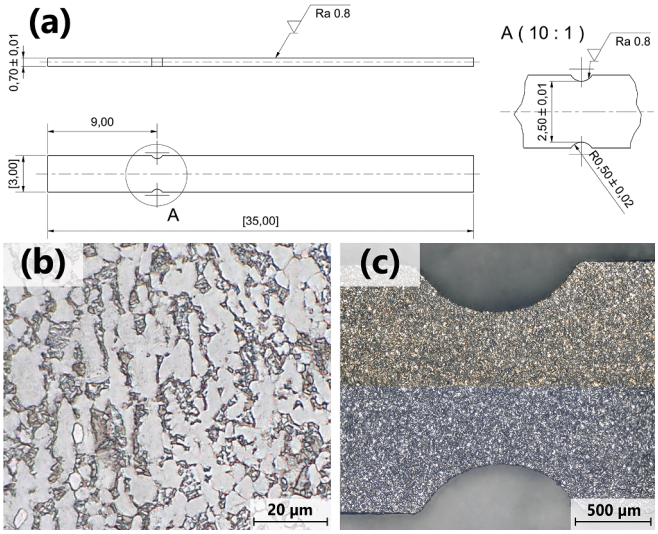

Fig. A1. (a) Dimensions of the custom-made Ti-6Al-4V fatigue specimen. (b) Light microscope image of the fully equiaxed microstructure of the fatigue specimens. In the polished and etched sample, the α-phase appears bright, while the β-phase appears dark. (c) Top-view digital microscope images of the notch region of a fatigue specimen (top) before and (bottom) after deposition of .

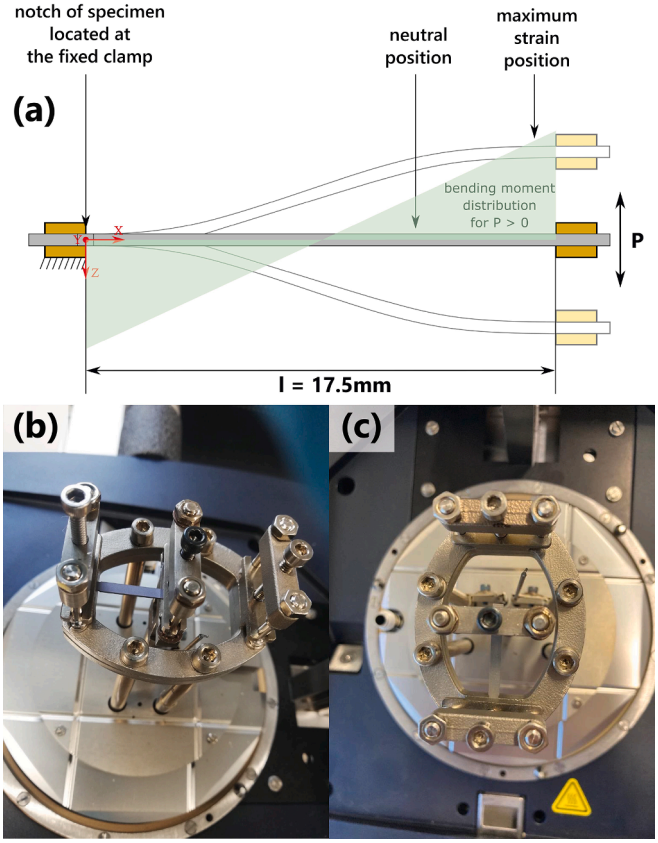

Fig. A2. (a) Schematic of the bending mode during single cantilever fatigue testing. (b) & (c) Images of the fully mounted DMA test configuration.

Data availability

Data will be made available on request.

References

[1] M. Peters, J. Kumpfert, C.H. Ward, C. Leyens, Titanium alloys for aerospace applications. Titanium and Titanium Alloys, Weinheim, FRG: Wiley-VCH Verlag GmbH & Co. KGaA, 2005, pp. 333–350, doi:10.1002/3527602119.ch13.

[2] K.G. Budinski, Tribological properties of titanium alloys, Wear 151 (1991) 203–217, https://doi.org/10.1016/0043-1648(91)90249-T.
[3] D. Siva Rama Krishna, Y.L. Brama, Y. Sun, Thick rutile layer on titanium for tribological applications, Tribol. Int. 40 (2007) 329–334, https://doi.org/10.1016/j.triboint.2005.08.004.
[4] J.T. Philip, J. Mathew, B. Kuriachen, Tribology of Ti6Al4V: a review, Friction 7 (2019) 497–536, https://doi.org/10.1007/s40544-019-0338-7.
[5] H. Dong, T. Bell, Enhanced wear resistance of titanium surfaces by a new thermal oxidation treatment, Wear 238 (2000) 131–137, https://doi.org/10.1016/S0043-1648(99)00359-2.
[6] P.H. Mayrhofer, R. Rachbauer, D. Holec, F. Rovere, J.M. Schneider, 4.14 - protective transition metal nitride coatings, in: S. Hashmi, G.F. Batalha, C.J. Van Tyne, B. Yilbas (Eds.), Comprehensive Materials Processing, Elsevier, Oxford, 2014, pp. 355–388, 10.1016/B978-0-08-096532-1.00423-4.
[7] R. Hollerweger, H. Riedl, J. Paulitsch, M. Arndt, R. Rachbauer, P. Polcik, et al., Origin of high temperature oxidation resistance of Ti–Al–Ta–N coatings, Surf. Coat. Technol. 257 (2014) 78–86, https://doi.org/10.1016/j.surfcoat.2014.02.067.
[8] S. PalDey, S.C. Deevi, Single layer and multilayer wear resistant coatings of (Ti,Al)N: a review, Mater. Sci. Eng. A 342 (2003) 58–79, https://doi.org/10.1016/S0921-5093(02)00259-9.
[9] V.F.C. Sousa, F.J.G. Da Silva, G.F. Pinto, A. Baptista, R. Alexandre, Characteristics and wear mechanisms of TiAlN-based coatings for machining applications: a comprehensive review, Metals 11 (2021) 260, https://doi.org/10.3390/met11020260.
[10] K. Balasubramanian, S.V. Khare, D. Gall, Valence electron concentration as an indicator for mechanical properties in rocksalt structure nitrides, carbides and carbonitrides, Acta Mater. 152 (2018) 175–185, https://doi.org/10.1016/j.actamat.2018.04.033.
[11] R.O. Ritchie, Mechanisms of fatigue-crack propagation in ductile and brittle solids, Int. J. Fract. 100 (1999) 55–83, https://doi.org/10.1023/A:1018655917051.
[12] M.E. Launey, R.O. Ritchie, On the fracture toughness of advanced materials, Adv. Mater. 21 (2009) 2103–2110, https://doi.org/10.1002/adma.200803322.
[13] L. Zauner, R. Hahn, E. Aschauer, T. Wojcik, A. Davydok, O. Hunold, et al., Assessing the fracture and fatigue resistance of nanostructured thin films, Acta Mater. 239 (2022) 118260, https://doi.org/10.1016/j.actamat.2022.118260.
[14] N.P. Sivagnanam Chandra, Y. Otsuka, Y. Mutoh, K. Yamamoto, Fatigue strength and mechanism of Ti6242S titanium alloy with TiAlN coating deposited under various bias voltages, Int. J. Fatigue 131 (2020) 105338, https://doi.org/10.1016/j.ijfatigue.2019.105338.
[15] N.P. Sivagnanam Chandra, Y. Otsuka, Y. Mutoh, K. Yamamoto, Effect of coating thickness on fatigue behavior of TiAlN coated Ti-alloys, Int. J. Fatigue 140 (2020) 105767, https://doi.org/10.1016/j.ijfatigue.2020.105767.
[16] Z. Zhang, Y. Zhang, Z. Zhang, G. He, Effect of brittle TiN coating on fatigue performance of TC11 titanium alloy under rotating bending and tension-tension, J. Alloys Compd. 968 (2023) 172163, https://doi.org/10.1016/j.jallcom.2023.172163.
[17] Y. Bai, T. Guo, J. Wang, J. Gao, K. Gao, X. Pang, Stress-sensitive fatigue crack initiation mechanisms of coated titanium alloy, Acta Mater. 217 (2021) 117179, https://doi.org/10.1016/j.actamat.2021.117179.
[18] Y. Bai, Y. Xi, K. Gao, H. Yang, X. Pang, X. Yang, et al., Brittle coating effects on fatigue cracks behavior in Ti alloys, Int. J. Fatigue 125 (2019) 432–439, https://doi.org/10.1016/j.ijfatigue.2019.04.017.
[19] M.Y.P. Costa, M.L.R. Venditti, M.O.H. Cioffi, H.J.C. Voorwald, V.A. Guimarães, R. Ruas, Fatigue behavior of PVD coated Ti–6Al–4V alloy, Int. J. Fatigue 33 (2011) 759–765, https://doi.org/10.1016/j.ijfatigue.2010.11.007.
[20] T. Guo, L. Qiao, X. Pang, A.A. Volinsky, Brittle film-induced cracking of ductile substrates, Acta Mater. 99 (2015) 273–280, https://doi.org/10.1016/j.actamat.2015.07.059.
[21] J. Wang, T. Guo, Y. Chen, X. Wang, P. Geng, K. Gao, et al., Significant improvement in fatigue life of titanium alloy induced by superlattice coating, Int. J. Fatigue 167 (2023) 107367, https://doi.org/10.1016/j.ijfatigue.2022.107367.
[22] B.S. Saini, V.K. Gupta, Effect of WC/C PVD coating on fatigue behaviour of case carburized SAE8620 steel, Surf. Coat. Technol. 205 (2010) 511–518, https://doi.org/10.1016/j.surfcoat.2010.07.022.
[23] G. Cassar, J.C. Avelar-Batista Wilson, S. Banfield, J. Housden, M. Fenech, A. Matthews, et al., Evaluating the effects of plasma diffusion processing and duplex diffusion/PVD-coating on the fatigue performance of Ti–6Al–4V alloy, Int. J. Fatigue 33 (2011) 1313–1323, https://doi.org/10.1016/j.ijfatigue.2011.04.004.
[24] E. Puchicabrera, M. Staia, J. Lesage, L. Gil, C. Villalobosgutierrez, J. Labarberasosa, et al., Fatigue behavior of AA7075-T6 aluminum alloy coated with ZrN by PVD, Int. J. Fatigue 30 (2008) 1220–1230, https://doi.org/10.1016/j.ijfatigue.2007.09.001.
[25] W.C. Oliver, G.M. Pharr, An improved technique for determining hardness and elastic modulus using load and displacement sensing indentation experiments, J. Mater. Res. 7 (1992) 1564–1583, https://doi.org/10.1557/JMR.1992.1564.
[26] A.C. Fischer-Cripps, Critical review of analysis and interpretation of nanoindentation test data, Surf. Coat. Technol. 200 (2006) 4153–4165, https://doi.org/10.1016/j.surfcoat.2005.03.018.
[27] S. Brinckmann, K. Matoy, C. Kirchlechner, G. Dehm, On the influence of microcantilever pre-crack geometries on the apparent fracture toughness of brittle materials, Acta Mater. 136 (2017) 281–287, https://doi.org/10.1016/j.actamat.2017.07.014.
[28] K. Matoy, H. Schönherr, T. Detzel, T. Schöberl, R. Pippan, C. Motz, et al., A comparative micro-cantilever study of the mechanical behavior of silicon based passivation films, Thin Solid Films 518 (2009) 247–256, https://doi.org/10.1016/j.tsf.2009.07.143.
[29] M. Birkholz, Thin_Film_Analysis_by_X-ray_scattering, Available: Wiley-VCH Verlag GmbH (2006) https://openlibrary.org/books/OL28983719M/Thin_Film_Analysis_by_X-Ray_Scattering.
[30] T. Degen, M. Sadki, E. Bron, U. König, G. Nénert, The highscore suite, Powder Diffr. 29 (2014) S13–S18.
[31] F. Tasnádi, M. Odén, I.A. Abrikosov, Ab initio elastic tensor of cubic $Ti_{0.5}Al_{0.5}N$ alloys: Dependence of elastic constants on size and shape of the supercell model and their convergence, Phys. Rev. B Condens. Matter 85 (2012) 144112, https://doi.org/10.1103/PhysRevB.85.144112.
[32] T. Gnäupel-Herold, ISODEC: software for calculating diffraction elastic constants, J. Appl. Crystallogr. 45 (2012) 573–574, https://doi.org/10.1107/S0021889812014252.
[33] P. van der Heide, Secondary Ion Mass Spectrometry: An Introduction to Principles and Practices, John Wiley & Sons, Inc., Hoboken, NJ, USA, 2014, pp. 350–357, 10.1002/9781118916780.refs.
[34] A. Benninghoven, Chemical analysis of inorganic and organic surfaces and thin films by static time-of-flight secondary ion mass spectrometry (TOF-SIMS), Angew. Chem. Int. Ed. Engl. 33 (1994) 1023–1043, https://doi.org/10.1002/anie.199410231.
[35] M. Kubicek, G. Holzlechner, A.K. Opitz, S. Larisegger, H. Hutter, J. Fleig, A novel ToF-SIMS operation mode for sub 100 nm lateral resolution: Application and performance, Appl. Surf. Sci. 289 (2014) 407–416, https://doi.org/10.1016/j.apsusc.2013.10.177.
[36] S.A. Nikulin, V.A. Markelov, A.Y. Gusev, T.A. Nechaykina, A.B. Rozhnov, S. O. Rogachev, et al., Low-cycle fatigue tests of zirconium alloys using a dynamic mechanical analyzer, Int. J. Fatigue 48 (2013) 187–191, https://doi.org/10.1016/j.ijfatigue.2012.10.019.
[37] S.A. Nikulin, A.B. Rozhnov, A.Y. Gusev, T.A. Nechaykina, S.O. Rogachev, M. Y. Zadorozhnyy, Fracture resistance of Zr–Nb alloys under low-cycle fatigue tests, J. Nucl. Mater. 446 (2014) 10–14, https://doi.org/10.1016/j.jnucmat.2013.11.039.
[38] A.B. Rozhnov, V.I. Pantsyrny, A.V. Kraynev, S.O. Rogachev, S.A. Nikulin, N. E. Khlebova, et al., Low-cycle bending fatigue and electrical conductivity of high-strength Cu/Nb nanocomposite wires, Int. J. Fatigue 128 (2019) 105188, https://doi.org/10.1016/j.ijfatigue.2019.105188.
[39] S.A. Nikulin, S.O. Rogachev, A.B. Rozhnov, V.I. Pantsyrnyi, N.E. Khlebova, T. A. Nechaykina, et al., Microstructure and fatigue strength of high-strength Cu–Fe and Cu–V in-situ nanocomposite wires, Compos. B 70 (2015) 92–98, https://doi.org/10.1016/j.compositesb.2014.10.046.
[40] M.S. de Oliveira Araújo, E.N.D. Grassi, C.J. de Araújo, Fatigue tests of superelastic NiTi wires: an analysis using factorial design in single cantilever bending, Smart Mater. Struct. 30 (2021) 125017, https://doi.org/10.1088/1361-665X/ac2f82.
[41] Neuber H. Kerbspannungslehre. Springer Berlin Heidelberg; doi:10.1007/978-3-642-56793-3.
[42] J. Keckes, M. Bartosik, R. Daniel, C. Mitterer, G. Maier, W. Ecker, et al., X-ray nanodiffraction reveals strain and microstructure evolution in nanocrystalline thin films, Scr. Mater. 67 (2012) 748–751, https://doi.org/10.1016/j.scriptamat.2012.07.034.
[43] G. Benecke, W. Wagermaier, C. Li, M. Schwartzkopf, G. Flucke, R. Hoerth, et al., A customizable software for fast reduction and analysis of large X-ray scattering data sets: applications of the new DPDAK package to small-angle X-ray scattering and grazing-incidence small-angle X-ray scattering, J. Appl. Crystallogr. 47 (2014) 1797–1803, https://doi.org/10.1107/S1600576714019773.
[44] Zauner L. A Matlab Toolbox for Synchrotron Stress Analysis. Feburary 23,2022. doi:10.5281/zenodo.6248169.
[45] M. Storm, pydidas - Python Diffraction Data Analysis Suite, Helmholtz-Zentrum Hereon (2024), https://doi.org/10.5281/zenodo.7568610.
[46] M. Stefenelli, J. Todt, A. Riedl, W. Ecker, T. Müller, R. Daniel, et al., X-ray analysis of residual stress gradients in TiN coatings by a Laplace space approach and cross-sectional nanodiffraction: a critical comparison, J. Appl. Crystallogr. 46 (2013) 1378–1385, https://doi.org/10.1107/S0021889813019535.
[47] Q. Chen, L. Liu, C. Zhu, K. Chen, Mesomechanical modeling and numerical simulation of the diffraction elastic constants for Ti6Al4V polycrystalline alloy, Metals 8 (2018) 822, https://doi.org/10.3390/met8100822.
[48] L. Zauner, Insights on the fracture and fatigue resistance of physical vapor deposited thin films, Technische Universität Wien. (2022), https://doi.org/10.34726/HSS.2022.66320.
[49] W.M. Seidl, M. Bartosik, S. Kolozsvári, H. Bolvardi, P.H. Mayrhofer, Influence of Ta on the fracture toughness of arc evaporated Ti-Al-N, Vacuum 150 (2018) 24–28, https://doi.org/10.1016/j.vacuum.2018.01.028.
[50] A. Hemmati, M. Abdoos, S.C. Veldhuis, Developing Ti-Al-Ta-N based coatings: thermal stability, oxidation resistance, machining performance and adaptive behavior under extreme tribological conditions, Mater. Today Commun. 31 (2022) 103373, https://doi.org/10.1016/j.mtcomm.2022.103373.
[51] A.R. Shugurov, E.D. Kuzminov, A.M. Kasterov, A.V. Panin, A.I. Dmitriev, Tuning of mechanical properties of Ti1−xAlxN coatings through Ta alloying, Surf. Coat. Technol. 382 (2020) 125219, https://doi.org/10.1016/j.surfcoat.2019.125219.
[52] R. Rachbauer, D. Holec, P.H. Mayrhofer, Increased thermal stability of Ti–Al–N thin films by Ta alloying, Surf. Coat. Technol. 211 (2012) 98–103, https://doi.org/10.1016/j.surfcoat.2011.07.009.
[53] C.M. Koller, R. Hollerweger, C. Sabitzer, R. Rachbauer, S. Kolozsvári, J. Paulitsch, et al., Thermal stability and oxidation resistance of arc evaporated TiAlN, TaAlN, TiAlTaN, and TiAlN/TaAlN coatings, Surf. Coat. Technol. 259 (2014) 599–607, https://doi.org/10.1016/j.surfcoat.2014.10.024.
[54] M. Mikula, M. Truchlý, D.G. Sangiovanni, D. Plašienka, T. Roch, M. Gregor, et al., Experimental and computational studies on toughness enhancement in Ti-Al-Ta-N

quaternaries, J. Vac. Sci. Technol. A (2017) 35, https://doi.org/10.1116/1.4997431.
[55] D. Holec, R. Rachbauer, L. Chen, L. Wang, D. Luef, P.H. Mayrhofer, Phase stability and alloy-related trends in Ti–Al–N, Zr–Al–N and Hf–Al–N systems from first principles, Surf. Coat. Technol. 206 (2011) 1698–1704, https://doi.org/10.1016/j.surfcoat.2011.09.019.
[56] W.-D. Münz, Titanium aluminum nitride films: a new alternative to TiN coatings, J. Vac. Sci. Technol. A 4 (1986) 2717–2725, https://doi.org/10.1116/1.573713.
[57] O. Knotek, M. Böhmer, T. Leyendecker, On structure and properties of sputtered Ti and Al based hard compound films, J. Vac. Sci. Technol. A 4 (1986) 2695–2700, https://doi.org/10.1116/1.573708.
[58] P.H. Mayrhofer, A. Hörling, L. Karlsson, J. Sjölén, T. Larsson, C. Mitterer, et al., Self-organized nanostructures in the Ti–Al–N system, Appl. Phys. Lett. 83 (2003) 2049–2051, https://doi.org/10.1063/1.1608464.
[59] G.S. Schajer, Practical residual stress measurement methods, John Wiley & Sons Inc., Chichester, West Sussex, United Kingdom, 2013, 10.1002/9781118402832.
[60] T. Ungár, Microstructural parameters from X-ray diffraction peak broadening, Scr. Mater. 51 (2004) 777–781, https://doi.org/10.1016/j.scriptamat.2004.05.007.
[61] ICDD. Powder Diffraction File - cubic AlN - 04-004-8344. 1996.
[62] ICDD. Powder Diffraction File - cubic TiN - 04-001-2272. 2020.
[63] ICDD. Powder Diffraction File - α-Ti - 01-071-4632. 1921.
[64] ICDD. Powder Diffraction File - Ti-6Al-4V - 04-002-8708. 2005.
[65] B. Grossmann, N. Schalk, C. Czettl, M. Pohler, C. Mitterer, Phase composition and thermal stability of arc evaporated Ti1 − xAlxN hard coatings with $0.4 \leq x \leq 0.67$, Surf. Coat. Technol. 309 (2017) 687–693, https://doi.org/10.1016/j.surfcoat.2016.11.015.
[66] H. Waldl, M. Tkadletz, A. Lechner, C. Czettl, M. Pohler, N. Schalk, Evolution of the fracture properties of arc evaporated Ti1-xAlxN coatings with increasing Al content, Surf. Coat. Technol. 444 (2022) 128690, https://doi.org/10.1016/j.surfcoat.2022.128690.
[67] G. Abadias, E. Chason, J. Keckes, M. Sebastiani, G.B. Thompson, E. Barthel, et al., Review Article: stress in thin films and coatings: current status, challenges, and prospects, J. Vac. Sci. Technol. A 36 (2018) 020801, https://doi.org/10.1116/1.5011790.
[68] X. Chen, Y. Du, Y.-W. Chung, Commentary on using H/E and H3/E2 as proxies for fracture toughness of hard coatings, Thin Solid Films 688 (2019) 137265, https://doi.org/10.1016/j.tsf.2019.04.040.
[69] M. Bartosik, C. Rumeau, R. Hahn, Z.L. Zhang, P.H. Mayrhofer, Fracture toughness and structural evolution in the TiAlN system upon annealing, Sci. Rep. 7 (2017) 16476, https://doi.org/10.1038/s41598-017-16751-1.
[70] T. Guo, Y. Chen, R. Cao, X. Pang, J. He, L. Qiao, Cleavage cracking of ductile-metal substrates induced by brittle coating fracture, Acta Mater. 152 (2018) 77–85, https://doi.org/10.1016/j.actamat.2018.04.017.
[71] M. Huff, Review paper: residual stresses in deposited thin-film material layers for micro- and nano-systems manufacturing, Micromachines (Basel) 13 (2022), https://doi.org/10.3390/mi13122084.
[72] M. Bartosik, D. Holec, D. Apel, M. Klaus, C. Genzel, J. Keckes, et al., Thermal expansion of Ti-Al-N and Cr-Al-N coatings, Scr. Mater. 127 (2017) 182–185, https://doi.org/10.1016/j.scriptamat.2016.09.022.
[73] P. Hidnert, Thermal expansion of titanium, J. Res. Natl. Bur. Stand. 30 (1943), https://doi.org/10.6028/jres.030.008.
[74] P.A.T. Olsson, I. Awala, J. Holmberg-Kasa, A.M. Krause, M. Tidefelt, O. Vigstrand, et al., Grain size-dependent thermal expansion of nanocrystalline metals, Materials 16 (2023), https://doi.org/10.3390/ma16145032.
[75] B.B. Panigrahi, V.V. Dabhade, M.M. Godkhindi, Thermal expansion behaviour of nanocrystalline titanium powder compacts, Mater. Lett. 59 (2005) 2539–2541, https://doi.org/10.1016/j.matlet.2005.03.041.
[76] R. Koch, The intrinsic stress of polycrystalline and epitaxial thin metal films, J. Phys. Condens. Matter 6 (1994) 9519–9550, https://doi.org/10.1088/0953-8984/6/45/005.
[77] L.B. Freund, S. Suresh, Thin Film Materials: Stress, Defect Formation and Surface Evolution, Cambridge University Press, 2004. Available: https://play.google.com/store/books/details?id=9UNnzNYAkboC.
[78] W.D. Nix, B.M. Clemens, Crystallite coalescence: a mechanism for intrinsic tensile stresses in thin films, J. Mater. Res. 14 (1999) 3467–3473, https://doi.org/10.1557/JMR.1999.0468.
[79] L. Vitos, A.V. Ruban, H.L. Skriver, J. Kollár, The surface energy of metals, Surf. Sci. 411 (1998) 186–202, https://doi.org/10.1016/S0039-6028(98)00363-X.
[80] C.C. Camilo, E.C. Souza, P.L. Di Lorenzo, Measurement of the grain boundary energy of commercially-pure grade 2 titanium at high temperature, Medida de energia de contorno de grão do titânio comercialmente puro – grau 2 – em alta temperatura 27 (2011) 175–181, https://doi.org/10.4322/rbeb.2011.014.
[81] S.C. Seel, C.V. Thompson, S.J. Hearne, J.A. Floro, Tensile stress evolution during deposition of Volmer–Weber thin films, J. Appl. Phys. 88 (2000) 7079–7088, https://doi.org/10.1063/1.1325379.
[82] Z. Rao, S. Berman, P. Yang, D. Depla, E. Chason, Understanding residual stress in thin films: Analyzing wafer curvature measurements for Ag, Cu, Ni, Fe, Ti, and Cr with a kinetic model, J. Appl. Phys. 130 (2021) 135304, https://doi.org/10.1063/5.0058919.
[83] E. Chason, T. Su, Z. Rao, Computational tool for analyzing stress in thin films, Surf. Coat. Technol. 474 (2023) 130099, https://doi.org/10.1016/j.surfcoat.2023.130099.
[84] G. Ongtrakulkij, J. Kajornchaiyakul, K. Kondoh, A. Khantachawana, Investigation of microstructure, residual stress, and hardness of Ti-6Al-4V after plasma nitriding process with different times and temperatures, Coat World. 12 (2022) 1932, https://doi.org/10.3390/coatings12121932.
[85] S. Spor, N. Jäger, M. Meindlhumer, H. Hruby, M. Burghammer, F. Nahif, et al., Evolution of structure, residual stress, thermal stability and wear resistance of nanocrystalline multilayered Al0.7Cr0.3N-Al0.67Ti0.33N coatings, Surf. Coat. Technol. 425 (2021) 127712, https://doi.org/10.1016/j.surfcoat.2021.127712.
[86] D.B. Lewis, I. Wadsworth, W.-D. Münz, R. Kuzel, V. Valvoda, Structure and stress of TiAlN/CrN superlattice coatings as a function of CrN layer thickness, Surf. Coat. Technol. 116–119 (1999) 284–291, https://doi.org/10.1016/S0257-8972(99)00132-2.
[87] W.M. Seidl, M. Bartosik, S. Kolozsvári, H. Bolvardi, P.H. Mayrhofer, Influence of coating thickness and substrate on stresses and mechanical properties of (Ti,Al,Ta)N/(Al,Cr)N multilayers, Surf. Coat. Technol. 347 (2018) 92–98, https://doi.org/10.1016/j.surfcoat.2018.04.060.
[88] C. Mendibide, P. Steyer, C. Esnouf, P. Goudeau, D. Thiaudière, M. Gailhanou, et al., X-ray diffraction analysis of the residual stress state in PVD TiN/CrN multilayer coatings deposited on tool steel, Surf. Coat. Technol. 200 (2005) 165–169, https://doi.org/10.1016/j.surfcoat.2005.02.081.
[89] C. Leyens, M. Peters, Titanium and Titanium Alloys: Fundamentals and Applications, Wiley-VCH; John Wiley, Weinheim, 2003.
[90] S. Baragetti, F. Tordini, A numerical study of the fatigue behaviour of notched PVD-coated Ti-6Al-4V, SDHM 3 (2007) 165–176, https://doi.org/10.3970/sdhm.2007.003.165.
[91] M.P. Echlin, J.C. Stinville, V.M. Miller, W.C. Lenthe, T.M. Pollock, Incipient slip and long range plastic strain localization in microtextured Ti-6Al-4V titanium, Acta Mater. 114 (2016) 164–175, https://doi.org/10.1016/j.actamat.2016.04.057.
[92] A. Ismaeel, D. Xu, X. Li, J. Zhang, R. Yang, Effect of texture on the mechanical and micromechanical properties of a dual-phase titanium alloy, J. Mater. Res. Technol. 27 (2023) 6833–6846, https://doi.org/10.1016/j.jmrt.2023.11.071.
[93] F. Benmessaoud, M. Cheikh, V. Velay, V. Vidal, H. Matsumoto, An optimization of the local Hall-Petch relationship using slip trace analysis technique and scale transition rules: Application in an equiaxed Ti-6Al-4V titanium alloy, Available, CIMNE (2019), http://hdl.handle.net/2117/182073.
[94] F. Aliaj, N. Syla, S. Avdiaj, T. Dilo, Effect of bias voltage on microstructure and mechanical properties of arc evaporated (Ti, Al)N hard coatings, Bull. Mater. Sci. (India) 36 (2013) 429–435, https://doi.org/10.1007/s12034-013-0479-7.